

Star-formation properties of Hickson Compact Groups based on deep $H\alpha$ imaging

Paul Eigenthaler¹, Sylvia Ploeckinger^{2,3}, Miguel Verdugo², Bodo Ziegler²

¹ Instituto de Astronomía y Astrofísica, Pontificia Universidad Católica de Chile, Av. Vicuña Mackenna 4860, Santiago, Chile

² Institut für Astrophysik, Universität Wien, Türkenschanzstraße 17, 1180 Wien, Austria

³ Leiden Observatory, Leiden University, PO Box 9513, NL-2300 RA Leiden, the Netherlands

email: eigenth@astro.puc.cl

xxx

ABSTRACT

We present deep $H\alpha$ imaging of seven Hickson Compact Groups (HCGs) using the 4.1m Southern Astrophysics Research (SOAR) Telescope. The high spatial resolution of the observations allow us to study both the integrated star-formation properties of the main galaxies as well as the 2D distribution of star-forming knots in the faint tidal arms that form during interactions between the individual galaxies. We derive star-formation rates and stellar masses for group members and discuss their position relative to the main sequence of star-forming galaxies. Despite the existence of tidal features within the galaxy groups, we do not find any indication for enhanced star-formation in the selected sample of HCGs. We study azimuthally averaged $H\alpha$ profiles of the galaxy disks and compare them with the g' and r' surface brightness profiles. We do not find any truncated galaxy disks but reveal that more massive galaxies show a higher light concentration in $H\alpha$ than less massive ones. We also see that galaxies that show a high light concentration in r' , show a systematic higher light concentration in $H\alpha$. TDG candidates have been previously detected in R -band images for 2 groups in our sample but we find that most of them are likely background objects as they do not show any emission in $H\alpha$. We present a new tidal dwarf galaxy (TDG) candidate at the tip of the tidal tail in HCG 91.

Key words: galaxies: groups: general — galaxies: interactions — galaxies: evolution — galaxies: photometry

1 INTRODUCTION

A key question in ongoing extragalactic research is to understand to what extent galaxy properties are determined by initial conditions (nature) or driven by environmental effects (nurture). Observations in the last few decades have revealed that the evolution of galaxies is indeed strongly dependent on their environment. In fact, most galaxies are not isolated, but found in gravitationally bound aggregates, such as groups or clusters (Tully 1987; Abell et al. 1989; Nolthenius 1993). Hence, to fully understand galaxy evolution and assess the relative importance of nature vs. nurture, it is essential to investigate the various physical processes in these different environments modifying galaxy properties such as star-formation rate (SFR), morphology, kinematics and color. In this context, compact groups of galaxies provide an ideal laboratory to study the effects of galaxy-galaxy interactions on the evolution of individual group members. Hickson (1982) defined a catalogue of 100 compact groups (hereafter Hickson Compact Groups, HCGs) with 451 galaxies in total. Although some galaxies in this sample turned out to be chance projections along the line-of-sight, not physically bound to the corresponding group, the Hickson (1982) sample is still the most detailed studied sample of compact groups

in the literature due to the vicinity of member galaxies at a median distance of $89 h^{-1}$ Mpc (Hickson et al. 1992). The comparatively low velocity dispersions in the order of 200 km s^{-1} and the high spatial density with a median projected galaxy separation of only $39 h^{-1}$ kpc (Hickson et al. 1992) make HCGs the perfect targets to investigate ongoing galaxy transformations due to galaxy-galaxy interactions. Based on their high spatial density and low velocity dispersions, crossing times for HCGs are short ($t_{\text{cr}} \leq 0.02 H_0^{-1}$; Diaferio et al. 1994) making their mere existence puzzling. In fact, dark matter simulations have shown that HCGs should merge into a single massive galaxy within a Gyr (Barnes 1985; Bode et al. 1993), being possibly the precursor of so-called fossil groups. One explanation for the existence of HCGs is that they have just recently formed and started to interact on short timescales. Mendes de Oliveira & Hickson (1994) studied the morphology of galaxies in 92 HCGs with at least three accordant members and found that 43% of all galaxies in their sample show morphological or kinematical distortions indicative of interactions or mergers while Hickson (1982) noted that the spiral fraction in HCGs is a factor of two lower than in field galaxies. These observations hint towards a scenario where galaxies in compact groups undergo frequent interactions and mergers, depleting late-type galaxies

while building up a higher early-type fraction instead. During this very dynamic stage it is possible to study the impact of the high density environment on the evolution of the individual group members, which is not yet fully understood. While interactions in galaxy pairs typically increase the SFR, e.g. due to a compressing tidal field (Renaud et al. 2009), no statistically significant increase in the specific star-formation rates (sSFR) of galaxies in HCGs has been found (Bitsakis et al. 2010). A possible explanation for the reduced SFR in HCGs is efficient gas stripping through ongoing tidal interactions, a process that is typical for the compact group environment. It has been shown that other possible mechanisms to suppress or even quench star-formation in HCGs are shocks and turbulence (Alatalo et al. 2014). Cluver et al. (2013) studied a sample of 74 galaxies in 23 Hickson Compact Groups (HCGs) and find evidence for enhanced warm H_2 emission in $\sim 20\%$ of these galaxies, most of which lie in the optical green valley between the blue cloud and red sequence. This emission has been associated with the dissipation of mechanical energy caused by a large-scale shock, induced when one group member collides at high velocity with tidal debris in the intragroup medium. Hence, shock excitation or turbulent heating are likely responsible for the enhanced H_2 emission in compact group galaxies and the suppression of star-formation. Other sources of heating like UV or X-ray excitation from star-formation or AGN activity are insufficient to account for the observed emission. Verdes-Montenegro et al. (2001) found a mean HI deficiency of 40 % for 48 HCGs and noted that groups with a higher early-type fraction or more compact systems with larger velocity dispersions tend to be more HI deficient. Desjardins et al. (2013) studied 9 HCGs in X-rays and have shown that HCGs with a higher X-ray luminosity show a lower sSFR. These observations suggest an evolutionary scenario where the amount of detected HI in galaxies, and hence the sSFR, decreases with evolution by continuous tidal stripping and/or gas heating to X-ray wavelengths. These distortions should also be reflected in the observed $H\alpha$ profiles of the galaxy disks, which are expected to be truncated based on the frequent interactions. Besides the distortion of gas disks within the galaxies, the ongoing interactions can also efficiently remove gas from its host galaxies, forming long filamentary structures and bridges (Iglesias-Páramo & Vilchez 2001; Serra et al. 2012). These arms can become the birthplace of a new generation of actively star-forming star clusters and so-called tidal dwarf galaxies (TDGs; see Duc 2012 and references therein). Hunsberger et al. (1996) listed 47 TDG candidates in 15 tidal features within HCGs and Hunsberger et al. (1998) showed that the faint end of the luminosity function is indeed enhanced in HCGs, possibly due to the efficient formation of TDGs. In this work we continue these studies and investigate the spatial distribution of ongoing star-formation in a sample of 7 HCGs in the southern hemisphere by performing deep $H\alpha$ imaging with the 4.1m SOAR telescope. Specifically we compare the integrated SFRs of group members with the main sequence of star-forming galaxies and analyze the azimuthally-averaged $H\alpha$ surface brightness profiles of the interacting galaxies. By comparing these profiles with the corresponding surface brightness profiles of the stellar component, we can reveal any distortions in the gas component of the galaxies caused by environmental effects such as tidal stripping. The deep observations also allow us to detect actively star-forming TDG candidates within the tidal tails of the interacting galaxies. For two groups in our sample, HCG26 and HCG96, we compare our $H\alpha$ maps with the work of Hunsberger et al. (1996), who claim to detect new TDG candidates in these systems based on deep R band images. All groups in our sample have been selected based

on their recession velocities ($cz \sim 8000 \text{ km s}^{-1}$) and morphological appearance, i.e. all groups show strong interactions between their brightest galaxies.

The paper is organised as follows. In Sect. 2 observations, data reduction and photometric measurements are described while Sect. 3 focuses on data analysis and presents all obtained results. Section 4 discusses individual groups and compares our findings with studies from the literature. Conclusions are given in Sect. 5. Magnitudes presented in this work are AB magnitudes except otherwise stated. Throughout the paper, the standard Λ CDM cosmology with $\Omega_M = 0.3$, $\Omega_\Lambda = 0.7$, and a Hubble constant of $H_0 = 70 \text{ km s}^{-1}$ is used.

2 OBSERVATIONS, DATA REDUCTION AND PHOTOMETRY

We carried out deep imaging at the 4.1m SOAR telescope during one night in 2013–October 10 in visitor mode, utilizing the Goodman spectrograph in imaging mode. The Goodman spectrograph consists of 4096×4096 pixels with a pixel size of $15\mu\text{m}$ yielding a spatial scale of $0.15 \text{ arcsec pixel}^{-1}$ in 1×1 imaging mode. This configuration corresponds to an effective circular field-of-view (FOV) of $\sim 7.2 \text{ arcmin}$ in diameter due to the assembly of the spectrograph slit changer. We chose Goodman instead of the SOAR Optical Imager (SOI) due to the slightly larger FOV and the higher throughput in all observed passbands. At the typical redshift of our group sample ($z \sim 0.03$), the observed FOV corresponds to a circular, physical area of $\sim 250 \text{ kpc}$ in diameter, covering the bright, central interacting galaxies of all our HCGs with only one pointing. The seeing ranged from 0.6 to 1.0 arcsec during the night, typically measuring 0.8 arcsec yielding a physical resolution of $\sim 500 \text{ pc}$ (see Table 1). To construct $H\alpha$ maps for our sample of HCGs, we obtained deep images in the S_{II} narrowband filter ($\lambda_{\text{eff}} = 6743\text{\AA}$, FWHM = 67\AA), matching the position of the $H\alpha$ line at the redshift of our targets. In addition, we took broadband images in SDSS r' , to estimate the continuum around the $H\alpha$ line, and in SDSS g' to obtain $g' - r'$ color information for all galaxies in our FOV. Figure 1 shows the corresponding filter transmission curves, as well as a spectral template of a starburst galaxy redshifted to the group distance of HCG04, part of our sample.

2.1 Data Reduction

For every compact group, we split the observations into individual dithered exposures to allow cosmic ray removal and correct for bad pixels. Table 1 summarizes the observations and lists all observed targets. We took bias and domeflats in the afternoon and skyflats during twilight. To calibrate our data photometrically we observed two standard star fields in g' and r' in SDSS Stripe 82 (Ivezić et al. 2007), one at the beginning, the other at the end of the night. To calibrate the S_{II} narrowband filter, we observed the spectrophotometric standard star LTT1020 (Hamuy et al. 1992, 1994) with this filter in the middle of the night. Data reduction was carried out within IRAF. To remove the instrument signature from our science frames, we first created a masterbias to remove the bias level including any two-dimensional structures. Masterflats were created in all filters by average combining the bias-corrected individual flat frames and normalizing the combined flats by the mode of the pixel distribution. Science frames were then flat-fielded and aligned spatially

Table 1. Sample of Hickson Compact Groups observed at the SOAR Telescope.

group	α_{2000}	δ_{2000}	z^a	v [km s $^{-1}$] ^a	D [Mpc] ^b	g'^c	r'^c	SII ^c	resolution ^d
HCG04	00 34 16.0	-21 26 48	0.0280	8277	123	360s	580s	1800s	450pc
HCG24	03 20 18.9	-10 51 53	0.0305	9004	134	360s	610s	1800s	488pc
HCG25	03 20 43.7	-01 03 07	0.0212	6288	92	360s	480s	1800s	343pc
HCG26	03 21 54.2	-13 38 45	0.0316	9324	139	360s	480s	1800s	505pc
HCG89	21 20 10.8	-03 54 32	0.0297	8772	130	360s	480s	1800s	476pc
HCG91	22 09 12.4	-27 46 33	0.0238	7050	104	160s	430s	1150s	384pc
HCG96	23 27 58.3	+08 46 27	0.0292	8626	128	320s	450s	1800s	468pc

Notes: ^a Redshifts and recession velocities taken from SIMBAD. ^b Luminosity distances have been computed with the Cosmology Calculator (Wright 2006). ^c Values show total exposure times for filters g' , r' and SII. ^d Spatial resolution in pc assuming an average seeing of 0.8 arcsec.

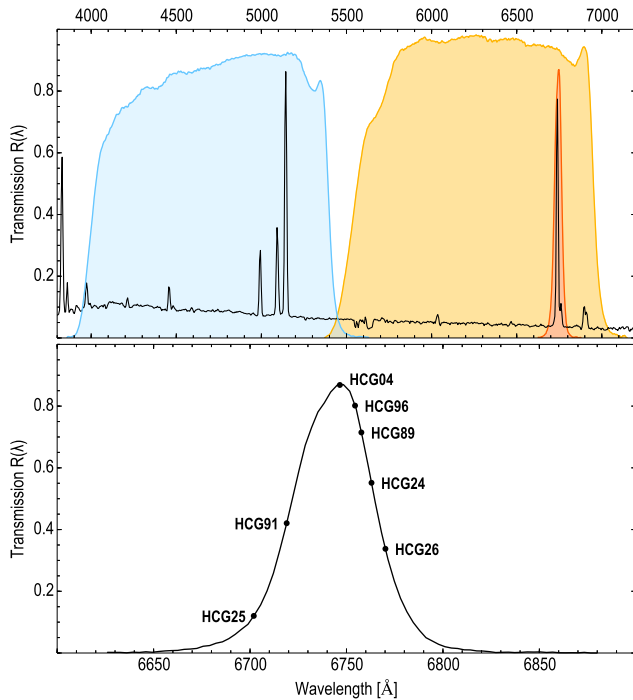


Figure 1. *Upper panel:* Transmission curves of the used filters. Blue: SDSS g' , yellow: SDSS r' , orange: SII narrowband. The black line indicates a spectral template of a starburst galaxy redshifted to the group distance of HCG04, part of our sample. The SII narrowband filter encompasses the [NII]–H α –[NII] triplet. The spectral template was taken from Calzetti et al. (1994). *Lower panel:* Filled circles mark the positions of the redshifted H α line in our group sample within the SII narrowband filter.

with the IRAF task `imalign` to correct for the 10 arcsec dither, previously introduced to avoid bad pixels. For all frames, the alignment was checked by eye, comparing the individual and co-added images. Before combining our images, we corrected the reduced and aligned science frames for cosmic rays utilizing the Laplacian edge detection technique `L.A.COSMIC` (van Dokkum 2001). This method proved to be efficient in detecting and removing cosmic rays from our images. Once all individual images had been cleaned from cosmic rays, we normalized all frames by the corresponding exposure times to obtain countrates. Subsequently, we average combined all individual frames rejecting 3σ outliers to account for any remaining cosmic ray artefacts not detected via `L.A.COSMIC`. We calibrated our science frames astrometrically within the `STARLINK GAIA`¹ pack-

age (Draper et al. 2009) by matching sources from the 2MASS catalog with the corresponding sources in our images until a deviation in the order of a negligible pixel fraction was achieved. The final calibration was checked by overplotting the 2MASS catalog on the resulting astrometrically calibrated science frames. We subtracted the sky from our images by computing the mode of the pixel distribution in each frame and subtracting it. This method proved to be adequate for our data since no spatial trends in the sky background were found in the observed FOV. Finally, the co-added frames from all three filters were aligned spatially with `imalign` so that the position of the observed sources match in each passband.

2.2 Photometric calibration

Photometric calibration was performed by computing photometric zeropoints via

$$m_{\text{SDSS}} = m_{\text{inst}} + Z_P - kX = -2.5 \log(\text{ADU/sec}) + Z_P - kX \quad (1)$$

where $m_{\text{inst}} = -2.5 \log(\text{ADU/sec})$ is the measured instrumental magnitude, m_{SDSS} the SDSS magnitude on the AB system (Oke & Gunn 1983), Z_P the photometric zeropoint, k the extinction coefficient, and X the airmass during exposure. To determine photometric zeropoints we measured instrumental magnitudes in SDSS g' and r' for all stars from the Ivezić et al. (2007) catalog falling in our two Stripe82 fields. We corrected for airmass considering extinction coefficients $k_{g'} = 0.12$ and $k_{r'} = 0.11$ determined for Cerro Pachón (Ryder et al. 2006). Following equation 1 we compute zeropoints $Z_{P,g'} = 26.56 \pm 0.12$ and $Z_{P,r'} = 26.53 \pm 0.08$. To calibrate the SII narrowband filter, we integrated the flux of the spectrophotometric standard star $f(\lambda)$ within the filter transmission $R_{\text{SII}}(\lambda)$ and compared this value with the extinction corrected measured countrates c_{SII} . To account for extinction in SII we utilized the r' band extinction coefficient. Following this procedure, we derive a zeropoint

$$\kappa = \frac{\int f(\lambda) R_{\text{SII}}(\lambda) d\lambda}{c_{\text{SII}} [\text{ADU/sec}]} \quad (2)$$

of $\kappa = 8.484 \times 10^{-17}$ ergs s $^{-1}$ cm $^{-2}$ ADU $^{-1}$.

2.3 Image analysis

To measure the net-countrate in the H α + [NII] lines, we first created continuum maps by scaling the observed countrates in the r' band to the SII narrowband filter. Then the net H α + [NII] counts are given by $c_{\text{H}\alpha+\text{[NII]}} = c_{\text{SII}} - n c_{r'}$, where $c_{r'}$ and c_{SII} are the countrates in the r' band and narrowband frames, respectively. We estimated the filter scaling factor n by measuring the fluxes of 89

¹ <http://starlink.jach.hawaii.edu>

field stars in both the r' band and SII frames, assuming that field stars show no $H\alpha$ + $[\text{NII}]$ emission and hence provide the same level of continuum in both filters. We measured an average flux ratio of $1/n = 29.05$. We checked this value by also computing the area under both filter transmission curves, i.e. numerically integrating over the corresponding filter transmission data. We used Simpson's rule for that purpose and computed a similar ratio of transmissivity between the two filters of $1/n \approx 29.03$, confirming our measurements. We checked the resulting $H\alpha$ + $[\text{NII}]$ maps by investigating the outer parts of early-type galaxies in our frames, not expected to show any $H\alpha$ + $[\text{NII}]$ emission.

We then converted countrates to physical fluxes using the following equation

$$F_{H\alpha+[\text{NII}],\text{obs.}} = \kappa \frac{c_{H\alpha+[\text{NII}],\text{corr.}}}{R_{\text{SII}}(H\alpha)} \quad (3)$$

where $c_{H\alpha+[\text{NII}],\text{corr.}}$ are the extinction corrected net $H\alpha$ + $[\text{NII}]$ countrates, κ the photometric zeropoint, and $R_{\text{SII}}(H\alpha)$ the sensitivity of the narrowband filter at the redshifted $H\alpha$ line. For bright $H\alpha$ sources, the contamination of the continuum in the broadband filter by $H\alpha$ cannot be neglected. We corrected for this contamination using the following relation:

$$F_{H\alpha+[\text{NII}],0} = F_{H\alpha+[\text{NII}],\text{obs.}} \left(1 + \frac{\int R_{\text{SII}}(\lambda)d\lambda}{\int R_{r'}(\lambda)d\lambda} \right) \quad (4)$$

where $F_{H\alpha+[\text{NII}],\text{obs.}}$ is the observed flux and $F_{H\alpha+[\text{NII}],0}$ the corrected one.

2.4 Flux measurements

We measured total galaxy magnitudes in g' and r' as well as $H\alpha$ + $[\text{NII}]$ fluxes utilizing the Aperture Photometry Tool² (APT) package (Laher et al. 2012). Aperture radii were defined so that the integrated, sky-subtracted galaxy flux reached a flat plateau in the outskirts of the aperture curve of growth. Any remaining sky level was corrected by subtracting the median sky counts measured within an annulus around each aperture. Interlopers within the galaxy aperture were masked by hand. To account for Galactic extinction we used the extinction maps from Schlafly & Finkbeiner (2011). For g' and r' we applied the corresponding extinction values as listed in NED. To compute the extinction in the [SII] filter, we considered the extinction law of Cardelli et al. (1989) which can be parameterized as

$$A_X = \alpha_X \cdot R_V \cdot E_{B-V} \quad (5)$$

where $R_V = 3.1$ is the extinction parameter, E_{B-V} the reddening from Schlafly & Finkbeiner (2011), and $\alpha_{[\text{SII}]} = 0.790$.

2.4.1 GALEX NUV and FUV measurements

To complement our observations with fluxes in the ultraviolet, we measured near-UV (NUV; $\lambda_{\text{eff}} = 2315.7\text{\AA}$) and far-UV (FUV; $\lambda_{\text{eff}} = 1538.6\text{\AA}$) magnitudes from the background subtracted intensity maps found in the GALEX GR6/7 Data Release³ with the same procedure as described above. Except for HCG26, NUV and FUV images were available for all groups in our sample. With a spatial

² <http://www.aperturephotometry.org>

³ <http://galex.stsci.edu/GR6/>

Table 2. GALEX NUV and FUV data.

group	survey ^a	exposure time
HCG04	AIS	107s
HCG24	MIS	2041s
HCG25	MIS	3375s
HCG26
HCG89	MIS	2427s
HCG91	AIS	191s
HCG96	NGS	1643s

Notes: ^a AIS – All Sky Imaging Survey.

MIS – Medium Imaging Survey.

NGS – Nearby Galaxies Survey.

Table 3. Detection limits.

group	g' ^a	r' ^a	NUV ^a	FUV ^a	$H\alpha$ + $[\text{NII}]$ ^b
HCG04	24.68	24.30	25.48	25.45	0.61
HCG24	24.88	24.10	26.71	26.55	0.99
HCG25	25.04	24.31	27.15	27.04	4.69
HCG26	24.99	24.25	1.55
HCG89	23.99	23.82	26.99	26.94	1.10
HCG91	23.88	24.08	25.64	25.81	1.86
HCG96	24.42	23.91	26.80	26.91	0.83

Notes: ^a g' , r' , NUV and FUV limits are given in mag arcsec⁻².

^b $H\alpha$ + $[\text{NII}]$ limits are given in 10^{-16} erg s⁻¹ cm⁻² arcsec⁻².

scale of 1.5 arcsec pixel⁻¹ and a spatial resolution (FWHM) of 4.2 arcsec (~ 2.5 kpc) in FUV and 5.3 arcsec (~ 3.2 kpc) in NUV, the UV images are coarse compared to our optical measurements. We computed NUV and FUV magnitudes considering GALEX zero-points $Z_{P,\text{FUV}} = 18.82$ and $Z_{P,\text{NUV}} = 20.08$. Galactic extinction was estimated as above with $\alpha_{\text{NUV}} = 2.808$ and $\alpha_{\text{FUV}} = 2.617$. We considered one extinction value for each group. Table 2 summarizes the utilized GALEX data.

2.4.2 Error bars

We estimated error bars within the APT photometry package based on equation 3 shown in Laher et al. (2012). To do so, we first computed the effective gain $\mathcal{G} = N \times t_{\text{exp}} \times G$ for each image, where N is the number of averaged frames, t_{exp} the average exposure time, and G the gain of the raw images. For all of our measurements in g' and r' , the error bars estimated this way are much smaller than the accuracy of the derived photometric zeropoints. Hence, we consider the uncertainty in the photometric calibration, 0.08 mag in r' and 0.12 mag in g' , as error estimate for all of our integrated g' and r' measurements (see Sect. 2.2). Consequently, we estimate an error of 0.14 mag for $g'-r'$ colours.

2.5 Detection limits

We estimated detection limits for the utilized g' , r' , NUV and FUV images and for the created $H\alpha$ + $[\text{NII}]$ maps. To do so, we sampled the scatter in the sky background of the corresponding frames with IRAF imexam and considered a value of 3σ as detection limit. Applying the appropriate zero-points and spatial scales we converted these limits to mag arcsec⁻² for g' , r' , NUV and FUV and to 10^{-16} erg s⁻¹ cm⁻² arcsec⁻² for the $H\alpha$ + $[\text{NII}]$ maps. The resulting detection limits are shown in Table 3.

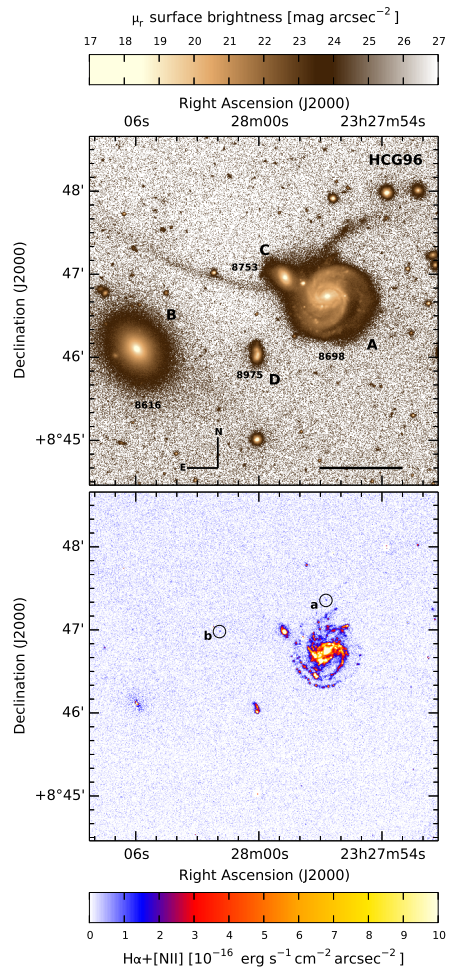


Figure 4. Same as Fig. 2 but for HCG96. Star-forming regions associated with tidal tails are marked with circles. See Sect. 3.6.

3 DATA ANALYSIS AND RESULTS

Table 4 shows the integrated, total g' , r' , NUV and FUV magnitudes as well as $g'-r'$ and $NUV-r'$ colors for all bright galaxies in our HCG sample. Figures 2, 3 and 4 show the observed r' band frames in mag arcsec^{-2} and the corresponding, continuum corrected $H\alpha+[NII]$ maps in $10^{-16} \text{ erg s}^{-1} \text{ cm}^{-2} \text{ arcsec}^{-2}$. We note that bright stars or the bright cores of some ellipticals produce artefacts in the created $H\alpha+[NII]$ maps possibly due to a different PSF in different passbands. When measured, these artefacts don't show any noteworthy $H\alpha+[NII]$ emission, however.

3.1 Compact group galaxies in the $NUV-r'$ plane

To distinguish between actively star-forming galaxies and passive quiescent galaxies, we constructed a $NUV-r'$ vs. M_r colour magnitude diagram (CMD). Figure 5 shows that our compact group galaxies are clearly separated in the $NUV-r'$ vs. M_r plane, following the well-defined blue and red sequences (dashed lines) for SDSS galaxies in the local universe (Wyder et al. 2007). We only find one galaxy, HCG96C, located in the green valley. From a total of 23 bright HCG member galaxies in our sample (for which we have NUV data), we find 12 galaxies ($\sim 52\%$) located in the blue

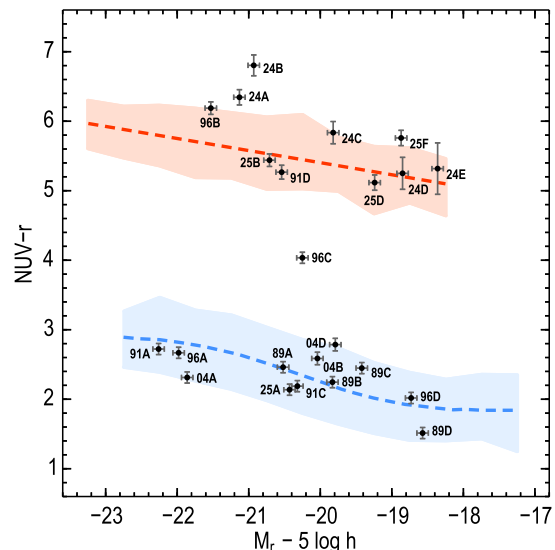


Figure 5. $NUV-r'$ vs. M_r colour-magnitude diagram for all observed compact group member galaxies. The dashed lines indicate the red and blue sequences for SDSS galaxies in the local universe derived by Wyder et al. (2007). Compact group members from our sample clearly fall on these sequences except for one outlier, HCG96C, located inside the green valley. The dashed areas show 1σ confidence intervals. The interlopers falsely classified as group members by Hickson (1982) are not shown in the plot.

sequence while we find 10 ($\sim 44\%$) located in the red sequence and one outlier ($\sim 4\%$) in the green valley. For our further analysis we only consider galaxies in the blue sequence as star-forming and unless otherwise stated compare only these star-formation rates with the literature. Since we do not have any UV data for HCG26, we use the $g'-r'$ color criterion proposed by Bell et al. (2003) for this system to distinguish star-forming and passive galaxies.

3.2 Star formation rates

To properly convert the measured $H\alpha+[NII]$ narrowband fluxes into star-formation rates, two corrections have to be taken into account. First, the narrowband fluxes have to be corrected for the contamination by the nitrogen $[NII]\lambda\lambda 6548, 6583$ lines. Second, the remaining $H\alpha$ fluxes have to be corrected for extinction due to dust within the observed galaxies. To apply these corrections, we utilize the following procedure.

Correcting for the contamination by the nitrogen $[NII]\lambda\lambda 6548, 6583$ lines is challenging since the correction factor $H\alpha/(H\alpha+[NII])$ can show a considerable scatter when measuring different HII regions within one galaxy. Based on the integrated $[NII]/H\alpha$ measurements of 58 galaxies from the SINGS survey (Kennicutt et al. 2003, 2009), we consider an average $H\alpha/(H\alpha+[NII])$ ratio of 0.74 ± 0.13 for the star-forming galaxies in our sample. We also checked if any of our galaxies is found in SDSS with spectroscopic measurements to verify this correction factor. We only found SDSS spectra for galaxies HCG25A and B and found that HCG25B hosts an AGN. For HCG25A we measured a $[NII]/H\alpha$ flux ratio of 0.69 which is in perfect agreement with the average value from the SINGS sample, proving the reliability of the applied correction factor.

Second, we account for $H\alpha$ extinction due to dust within the

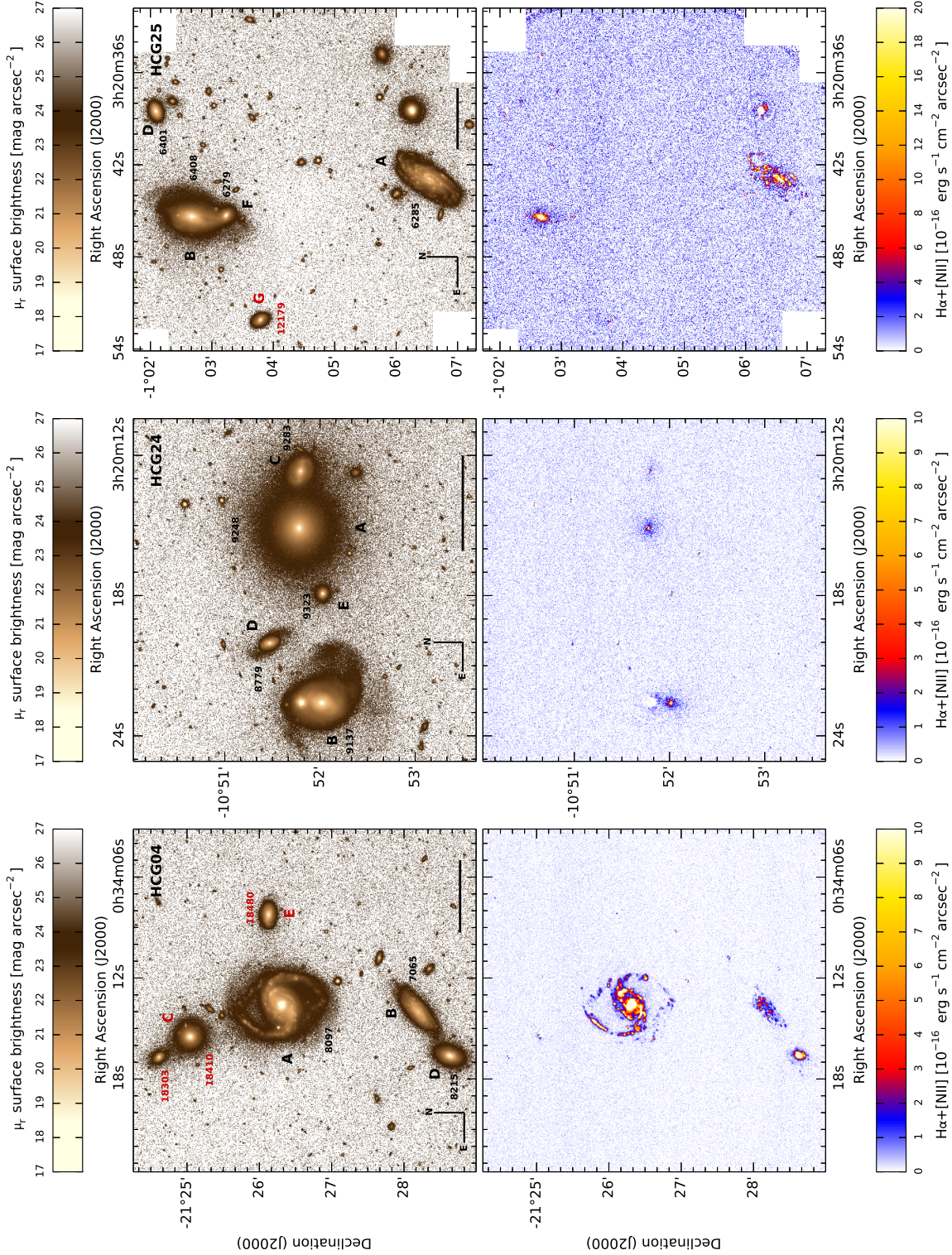


Figure 2. Observed Hickson Compact Groups in the r' band (top panels) and the corresponding continuum corrected $H\alpha+[NII]$ maps (lower panels). The colorscale for the r' band frames shows the proper surface brightness in mag arcsec^{-2} . Radial velocities of group members, taken from SIMBAD, are also shown. Galaxies with discordant redshifts are highlighted in red. The horizontal black lines indicate 1 arcmin. $H\alpha+[NII]$ fluxes are given in $10^{-16} \text{ erg s}^{-1} \text{ cm}^{-2} \text{ arcsec}^{-2}$.

observed galaxies. This correction is difficult since the dust fraction can vary strongly in galaxies of different morphological type and can even show a considerable scatter within a single galaxy. Recent studies have revealed a clear trend between $H\alpha$ extinction and stellar mass (Garn & Best 2010; Kashino et al. 2013), arguing

that the knowledge of stellar mass is sufficient to model the extinction of a galaxy in a statistical sense, i.e. once the mass dependence is applied, the accuracy of the extinction estimate cannot be improved significantly by a more complex model. We use the relation of Garn & Best (2010)

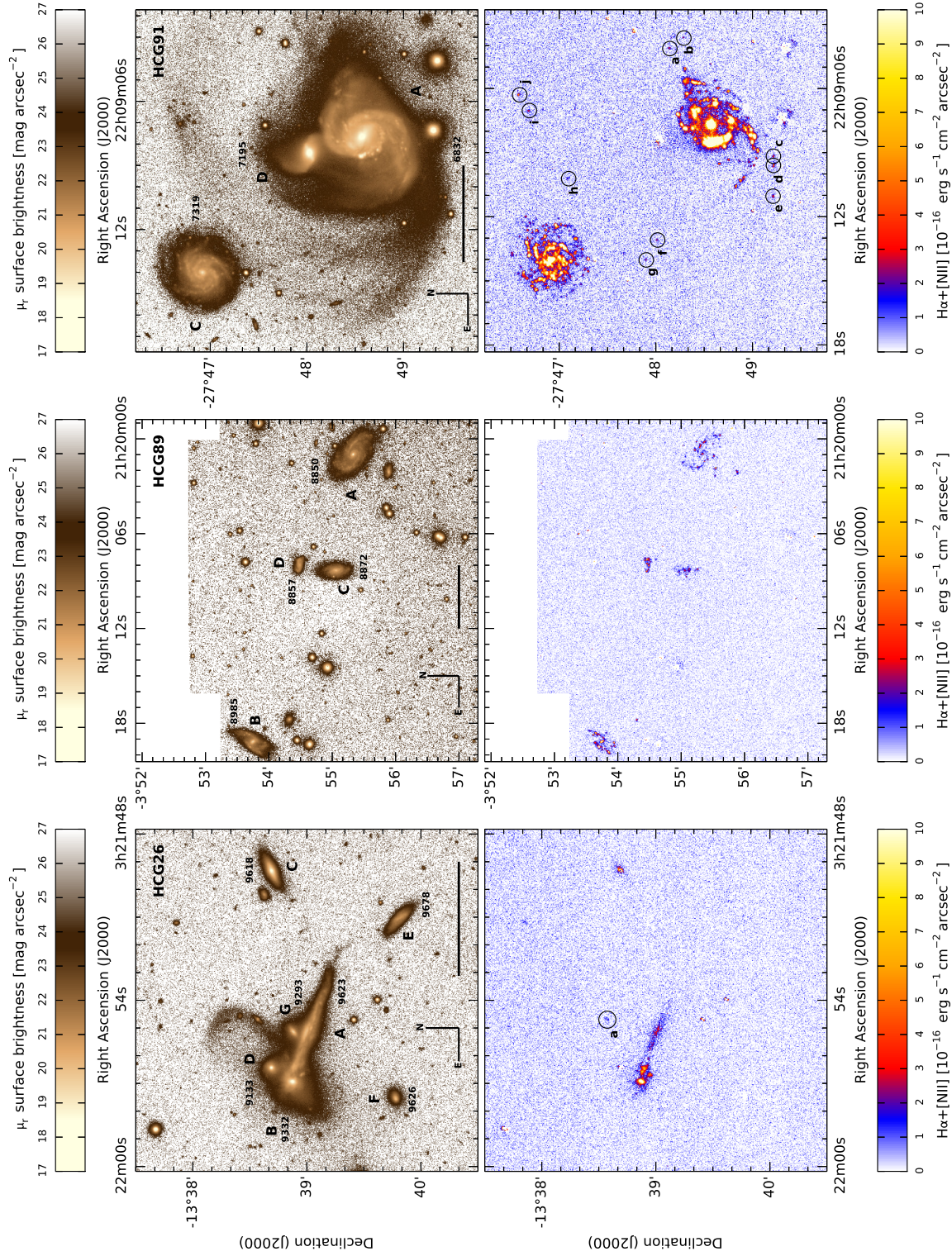


Figure 3. Same as Fig. 2 but for HCG26, HCG89, and HCG91. Star-forming regions associated with tidal tails are marked with circles. See Sect. 3.6.

$$A_{H\alpha} = 0.91 + 0.77X + 0.11X^2 - 0.09X^3 \quad (6)$$

to account for a stellar mass dependent H α dust extinction correction, where $X = \log(M_*/10^{10}M_\odot)$. The authors state an uncer-

tainty of 0.28 mag in $A_{H\alpha}$. The final corrected H α fluxes were subsequently converted to H α luminosities via:

$$L_{H\alpha} = 4r^2\pi F_{H\alpha} \quad (7)$$

where r is the corresponding luminosity distance in cm and

Table 4. Photometric measurements, radial velocities, and stellar masses of bright HCG galaxies.

group	galaxy	α_{2000}	δ_{2000}	g'^a [mag]	r'^a [mag]	$g'-r'^a$ [mag]	NUV [mag]	NUV- r' [mag]	v_r^b [km s ⁻¹]	$\log M_\star$ [M _⊙]	type ^d
HCG04	A	00 34 13.64	-21 26 19.0	13.26	12.82	0.44	15.13 ± 0.01	2.31 ± 0.08	8097	11.14 ± 0.06	Sc . (1)
	B	00 34 14.07	-21 28 12.0	15.15	14.64	0.52	17.22 ± 0.04	2.59 ± 0.09	7065	10.40 ± 0.07	Sb . (2)
	C	00 34 15.50	-21 25 03.0	15.38	14.61	0.77	21.02 ± 0.34	6.41 ± 0.35	18410 ^{ec}	11.41 ± 0.03	E2 . (1)
	D	00 34 16.65	-21 28 38.0	15.51	14.89	0.62	17.67 ± 0.05	2.79 ± 0.09	8215	10.44 ± 0.04	E4 . (1)
	E	00 34 08.27	-21 26 08.1	15.93	15.31	0.61	18.44 ± 0.06	3.13 ± 0.10	18480*	11.04 ± 0.06	Sab (2)
HCG24	A	03 20 15.14	-10 51 46.8	14.57	13.73	0.84	20.07 ± 0.08	6.34 ± 0.11	9248	11.19 ± 0.07	S0 . (2)
	B	03 20 22.61	-10 52 00.8	14.61	13.93	0.68	20.74 ± 0.13	6.80 ± 0.15	9137	11.04 ± 0.06	SBa (1)
	C	03 20 12.77	-10 51 47.8	16.05	15.04	1.01	20.88 ± 0.14	5.84 ± 0.16	9283	10.71 ± 0.23	SB0 (2)
	D	03 20 20.10	-10 51 28.8	16.53	16.02	0.51	21.27 ± 0.21	5.25 ± 0.23	8779	9.98 ± 0.06	S0a (2)
	E	03 20 17.93	-10 52 01.8	17.26	16.50	0.76	21.82 ± 0.36	5.32 ± 0.37	9323	10.04 ± 0.06	E . (2)
HCG25	A	03 20 42.95	-01 06 30.7	14.03	13.62	0.41	15.76 ± 0.01	2.14 ± 0.08	6285	10.50 ± 0.03	SBc (1)
	B	03 20 45.42	-01 02 40.8	14.29	13.34	0.96	18.78 ± 0.05	5.44 ± 0.09	6408	11.12 ± 0.09	SBa (1)
	D	03 20 38.81	-01 02 07.4	15.44	14.80	0.64	19.92 ± 0.07	5.12 ± 0.11	6401	10.25 ± 0.04	S0 . (1)
	F	03 20 45.35	-01 03 13.8	15.77	15.17	0.60	20.93 ± 0.07	5.76 ± 0.11	6279	10.15 ± 0.08	S0 . (1)
	G	03 20 52.10	-01 03 47.3	16.31	15.51	0.79	21.38 ± 0.13	5.86 ± 0.15	12179*	10.68 ± 0.06	S0 . (2)
HCG26	A	03 21 55.30	-13 39 03.1	15.26	14.69	0.58	9678	10.60 ± 0.01	Scd (1)
	B	03 21 57.15	-13 38 54.3	16.07	15.16	0.91	9332	10.79 ± 0.02	E0 . (1)
	C	03 21 49.42	-13 38 41.7	16.46	15.70	0.76	9618	10.39 ± 0.02	S0 . (2)
	D	03 21 56.50	-13 38 42.0	16.90	16.29	0.61	9133	10.01 ± 0.01	cI . (1)
	E	03 21 51.15	-13 39 48.5	17.26	16.82	0.44	9623	9.60 ± 0.01	Im . (1)
	F	03 21 57.65	-13 39 46.7	17.94	17.53	0.40	9626	9.27 ± 0.01	cI . (2)
	G	03 21 55.23	-13 38 55.5	17.62	16.88	0.74	9293	9.91 ± 0.01	S0 . (2)
HCG89	A	21 20 01.03	-03 55 19.6	14.70	14.28	0.43	16.74 ± 0.01	2.46 ± 0.08	8850	10.58 ± 0.04	Sc . (2)
	B	21 20 19.12	-03 53 45.6	15.44	14.96	0.47	17.21 ± 0.01	2.25 ± 0.08	8985	10.29 ± 0.05	SBc (1)
	C	21 20 08.31	-03 55 03.6	15.78	15.38	0.40	17.83 ± 0.02	2.45 ± 0.08	8872	10.14 ± 0.07	Scd (2)
	D	21 20 08.00	-03 54 30.0	16.41	16.23	0.18	17.74 ± 0.02	1.51 ± 0.08	8857	9.49 ± 0.01	Sm (2)
HCG91	A	22 09 07.69	-27 48 34.0	12.69	12.05	0.64	14.78 ± 0.01	2.72 ± 0.08	6832	11.50 ± 0.03	SBc (1)
	C	22 09 14.02	-27 46 56.0	14.46	13.99	0.47	16.18 ± 0.02	2.19 ± 0.08	7319	10.52 ± 0.03	Sc . (2)
	D	22 09 08.20	-27 48 01.0	14.54	13.77	0.77	19.04 ± 0.07	5.27 ± 0.10	7195	10.93 ± 0.01	SB0 (1)
HCG96	A	23 27 56.70	08 46 44.4	13.25	12.78	0.48	15.45 ± 0.01	2.67 ± 0.08	8698	11.34 ± 0.14	Sc . (1)
	B	23 28 05.95	08 46 07.4	14.12	13.23	0.89	19.42 ± 0.05	6.19 ± 0.09	8616	11.40 ± 0.06	E2 . (1)
	C	23 27 58.80	08 46 58.4	15.15	14.51	0.64	18.54 ± 0.02	4.03 ± 0.08	8753	10.78 ± 0.09	Sa . (1)
	D	23 28 00.20	08 46 02.0	16.41	16.03	0.38	18.05 ± 0.02	2.02 ± 0.08	8975	9.78 ± 0.01	Im . (1)

Notes: ^a We consider error bars of 0.08 mag in r' , 0.12 mag in g' , and 0.14 mag in $g'-r'$ (see Sect. 2.4.2 for details.) ^b Radial velocities taken from Hickson et al. (1992). Asterisks show nonmember galaxies originally classified as group members by Hickson (1982). ^c For HCG04C we list the radial velocity from SIMBAD, measured much more recently and showing a severe mismatch compared to the radial velocity given in Hickson et al. (1992) (8863 km s⁻¹). ^d (1): morphology taken from Mendes de Oliveira & Hickson (1994) — (2): morphology taken from SIMBAD.

$F_{\text{H}\alpha}$ the integrated $\text{H}\alpha$ flux of the whole galaxy. We computed star-formation rates in $M_\odot \text{ year}^{-1}$ by applying the calibration for $\text{H}\alpha$ fluxes as presented in Kennicutt & Evans (2012):

$$\log \dot{M}_\star [M_\odot \text{ year}^{-1}] = \log L_{\text{H}\alpha} [\text{erg s}^{-1}] - 41.27 \quad (8)$$

We estimated error bars considering the uncertainties in both the $\text{H}\alpha/(\text{H}\alpha + [\text{NII}])$ correction and the dust extinction since these error sources are considerably larger compared to the uncertainties in the flux measurements.

3.2.1 Correcting for AGN contamination

We checked the literature if any of our galaxies host an AGN to correct for any contamination in the measured emission line fluxes caused by non photo-ionization. Martínez et al. (2010) carried out a spectroscopic survey to identify AGNs in HCG galaxies, revealing that some of our objects indeed host an AGN. To get a more complete census of AGN contamination in our sample, we also searched the whole catalog of quasars and active nuclei from Véron-Cetty & Véron (2010) but could not find any additional AGNs. Based on our analysis of its SDSS spectrum, we measure $\log([\text{NII}]/\text{H}\alpha) = 0.26$

for the elliptical HCG25B. Comparing this value with the diagnostic diagram for emission line galaxies in Brinchmann et al. (2004), HCG25B can definitely be considered as AGN. Table 5 lists the activity type from Martínez et al. (2010) for the star-forming galaxies in our sample. Galaxies are classified as active galactic nuclei (AGN), transition objects (TO), and star-forming nuclei (SFN), where TOs are emission-line galaxies with line ratios intermediate between SFNs and AGNs. For galaxies hosting an AGN or TO we exclude the flux of the very center of each galaxy. Since the physical scale of an AGN is below our spatial resolution, we consider a central aperture matching the seeing of our observations, i.e. ~ 0.8 arcsec and subtract this flux from our integrated measurements.

3.2.2 Comparison with FUV

For comparison, we also derived star-formation rates from our FUV measurements. The main disadvantage of FUV as a tracer for star-formation is the strong FUV extinction due to interstellar dust. We correct for this attenuation considering FUV-NUV colors. According to Salim et al. (2007), FUV extinction A_{FUV} can be parametrized as

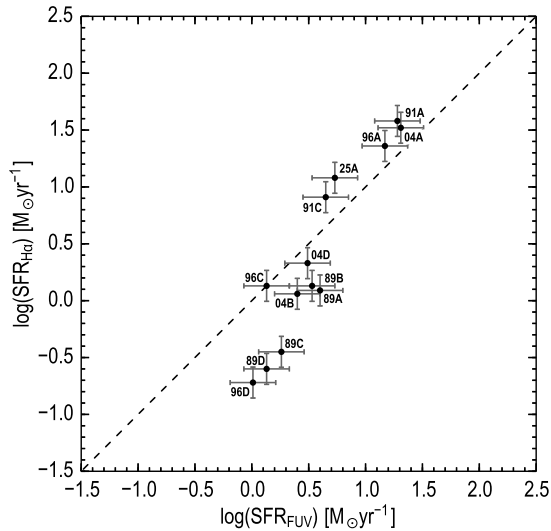


Figure 6. Comparison between FUV and $H\alpha$ star-formation rates for all compact group galaxies on the $NUV-r'$ blue sequence. There is a good agreement between $H\alpha$ and FUV star-formation rates for the brightest star-forming galaxies in our sample, while fainter galaxies show higher star-formation rates in FUV compared to $H\alpha$.

$$A_{FUV} = 2.99 \cdot (FUV - NUV) + 0.27 \quad (9)$$

for galaxies with $NUV-r' < 4$ and $(FUV - NUV) < 0.90$, which is true for all of our blue sequence objects. The typical scatter in A_{FUV} is 0.5 mag (Salim, private communication – cf. Fig. 13 in Salim et al. 2007), which we consider as the main error source for our FUV SFR estimates. After applying this dust extinction correction, we converted FUV_{AB} magnitudes to fluxes in $\text{erg s}^{-1} \text{cm}^{-2} \text{Hz}^{-1}$, then computed FUV luminosities in $\text{erg s}^{-1} \text{Hz}^{-1}$, and finally considered the relation of Salim et al. (2007)

$$\dot{M}_* [M_\odot \text{ year}^{-1}] = 1.08 \times 10^{-28} L_{FUV} [\text{erg s}^{-1} \text{Hz}^{-1}] \quad (10)$$

assuming a Salpeter IMF. Figure 6 shows the comparison of star-formation rates derived from integrated $H\alpha$ and FUV fluxes for all compact group galaxies in the $NUV-r'$ blue sequence while Table 5 lists all the corresponding values. We get a good agreement between $H\alpha$ and FUV star-formation rates for the brightest star-forming galaxies in our sample, while fainter galaxies show higher star-formation rates in FUV compared to $H\alpha$.

3.3 Galaxy stellar masses

We have estimated galaxy stellar masses by computing stellar mass-to-light ratios in various passbands based on the measured $g'-r'$ galaxy colors. According to Bell et al. (2003) stellar mass-to-light ratios can be parametrized by $g'-r'$ colors as

$$\log(M_*/L)_\odot = a_\lambda + b_\lambda \times (g' - r') \quad (11)$$

where the coefficients a_λ and b_λ define the relation for different passbands (see Table 7 in Bell et al. (2003) for the corresponding coefficients). We computed stellar mass-to-light ratios in g', r'

and also in the near-infrared JHK filters since 2MASS JHK magnitudes are available for most of our galaxies⁴. We derived galaxy luminosities in g', r', J, H, K considering absolute solar magnitudes measured by C. Willmer⁵. Based on the derived stellar mass-to-light ratios and galaxy luminosities, galaxy stellar masses were computed for every passband. Finally, we averaged the derived values and estimated error bars as the standard deviation of the individual measurements. Stellar masses are shown in Table 4.

3.4 Main sequence of star-forming galaxies

It is now widely known that star-forming galaxies show a tight correlation between their star-formation rates and stellar masses, forming a main sequence of star-forming galaxies in the $\log \text{SFR} - \log M_*$ plane

$$\log \text{SFR} [M_\odot \text{ yr}^{-1}] = \alpha \cdot \log M_* [M_\odot] + \beta \quad (12)$$

more massive galaxies exhibiting higher star-formation rates. The relation is evolving over cosmic time, with star-formation rates reaching maximum values at $z \sim 2 - 3$ at the peak of cosmic star-formation density and the slope α showing a possible evolution with redshift. In Fig. 7 we compare our measured star-formation and specific star-formation rates with the main sequence of local star-forming galaxies (Brinchmann et al. 2004, Elbaz et al. 2007, and Whitaker et al. 2012). The shaded areas show the 1σ scatter of these relations.

Only galaxies located in the $NUV-r'$ blue sequence are plotted, except for HCG25B, which based on its morphology and $NUV-r'$ color is an early-type galaxy (marked with a red dot) not expected to show any significant star-formation, but falls on the main sequence of star-forming galaxies. We see that almost all star-forming galaxies are located on the main sequence of local star-forming galaxies. Only galaxies HCG89C, HCG96C, and HCG96D are located below the 1σ thresholds of the various main sequences. Figure 7 also shows the relation between absolute r' band magnitudes and stellar mass. Considering equation 11, the scatter in the relation results from the fact that different galaxies show different $g - r$ colours and that the stellar masses shown are the computed averages of stellar mass estimates from various filter passbands.

3.4.1 Comparison with values from literature

To get an idea on the robustness of our stellar mass and star-formation estimates, we compare our measurements with the data from Bitsakis et al. (2014) who study several of our galaxies using multi-wavelength observations and SED fitting. Figure 8 shows the comparison of both datasets. Both stellar masses and star-formation rates from the present work are systematically above the Bitsakis et al. (2014) values with average offsets of 0.33 in $\log M_*$ and 0.46 in $\log \text{SFR}$. However, since *both* parameters are systematically above our values, datapoints shift along the main sequence of star-forming galaxies in the $\log \text{SFR} - \log M_*$ plane when considering the Bitsakis et al. (2014) values instead of ours, not affecting the interpretation of the present work (see Fig. 8c). The only two galaxies where we see a severe mismatch in star-formation rates are HCG25B and HCG96D.

⁴ We took JHK magnitudes from SIMBAD when available.

⁵ <http://mips.as.arizona.edu/~cna/w/sun.html>

Table 5. Star-formation rates of HCG member galaxies in the NUV-r blue sequence derived from H α and FUV fluxes.

group	galaxy	$\log F_{\text{H}\alpha+\text{NII}}^a$ [erg s $^{-1}$ cm $^{-2}$]	$\log L_{\text{H}\alpha}^b$ [erg s $^{-1}$]	$\log \text{SFR}_{\text{H}\alpha}^b$ [M $_{\odot}$ year $^{-1}$]	FUV [mag]	$\log L_{\text{FUV}}^c$ [erg s $^{-1}$ Hz $^{-1}$]	$\log \text{SFR}_{\text{FUV}}^c$ [M $_{\odot}$ year $^{-1}$]	$\log \text{SSFR}_{\text{H}\alpha}$ [Gyear $^{-1}$]	activity d
HCG04	A	-12.06	42.79	1.52	15.63 \pm 0.03	29.27	1.31	-0.62 \pm 0.15	TO
	B	-13.29	41.33	0.06	17.64 \pm 0.07	28.36	0.40	-1.34 \pm 0.15	TO
	D	-13.03	41.60	0.33	18.43 \pm 0.09	28.46	0.49	-1.11 \pm 0.14	SFN
HCG25	A	-12.05	42.35	1.08	16.16 \pm 0.01	28.70	0.73	-0.42 \pm 0.14	...
	B	-12.50	42.09	0.82	20.43 \pm 0.13	27.74	-0.23	-1.30 \pm 0.16	AGN*
HCG26 e	A	-13.33	41.46	0.19	-1.41 \pm 0.14	...
	A	-13.36	41.36	0.09	17.09 \pm 0.01	28.57	0.60	-1.49 \pm 0.14	...
	B	-13.23	41.40	0.13	17.73 \pm 0.02	28.50	0.53	-1.16 \pm 0.14	...
HCG89	C	-13.76	40.82	-0.45	18.30 \pm 0.03	28.22	0.26	-1.59 \pm 0.15	...
	D	-13.73	40.67	-0.60	18.01 \pm 0.02	28.10	0.13	-1.10 \pm 0.14	...
	A	-11.93	42.85	1.58	15.25 \pm 0.02	29.25	1.28	-0.92 \pm 0.14	AGN
HCG91	C	-12.33	42.18	0.91	16.58 \pm 0.03	28.62	0.65	-0.61 \pm 0.14	...
	A	-12.30	42.63	1.36	15.90 \pm 0.01	29.14	1.17	-0.98 \pm 0.19	AGN
HCG96	C	-13.37	41.40	0.13	19.24 \pm 0.04	28.09	0.13	-1.65 \pm 0.16	...
	D	-13.91	40.55	-0.72	18.35 \pm 0.03	27.97	0.01	-1.49 \pm 0.14	SFN

Notes: a We estimate an upper limit of 0.02 dex for the error in the $\log F_{\text{H}\alpha+\text{NII}}$ measurements. b We estimate an error of 0.14 dex in the $\log L_{\text{H}\alpha}$ and $\log \text{SFR}_{\text{H}\alpha}$ measurements based on the uncertainties of the applied corrections. c We consider an error of 0.20 dex in the $\log L_{\text{FUV}}$ and $\log \text{SFR}_{\text{FUV}}$ measurements based on the 0.5mag uncertainty of the dust correction. d Activity according to Martínez et al. (2010). SFN – star-forming nucleus, TO – transition object, AGN – active galactic nucleus. e We considered the $g'-r'$ color criterion of Bell et al. (2003) to identify blue, star-forming galaxies in this system.

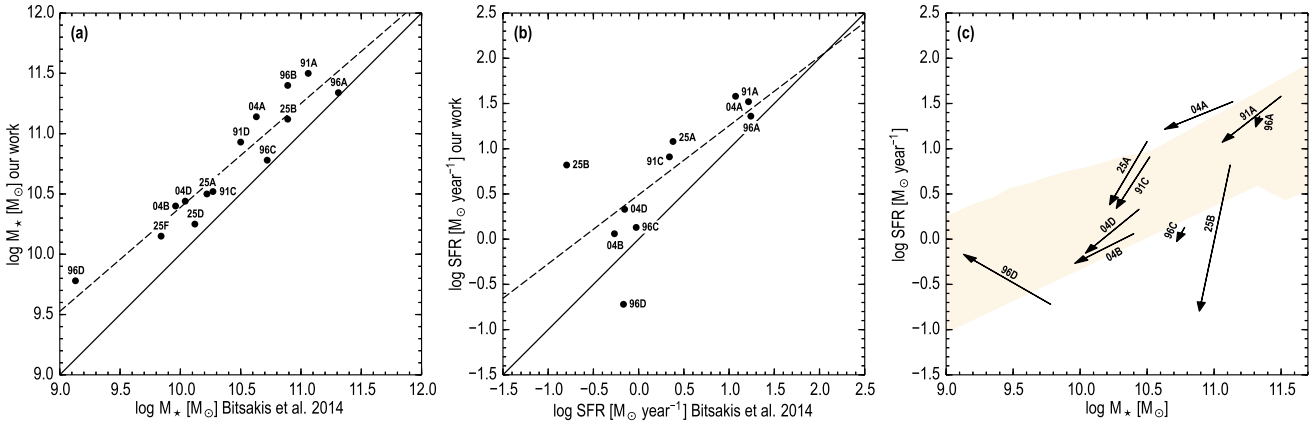


Figure 8. Comparison of the stellar masses and H α star-formation rates from the present work with Bitsakis et al. (2014). **a)** Stellar masses. The solid line indicates unity while the dashed line is a linear least squares fit to the data. Stellar masses from our work are systematically above the Bitsakis et al. (2014) ones with an average offset of 0.33 in $\log M_{\star}$. **b)** Same as panel **a)** but for star-formation rates. The star-formation rates from our work are again systematically above the Bitsakis et al. (2014) ones with an average offset of 0.46 in $\log \text{SFR}$. **c)** Arrows show the change of the position of the galaxies on the main sequence of star-forming galaxies when considering the Bitsakis et al. (2014) values instead of ours.

3.5 Spatial analysis of ionized gas and stellar populations

To study the spatial distribution of the H α emission tracing the ionized gas in the HCG member galaxies, we created H α +NII radial surface brightness profiles. In order to compare these profiles with the stellar component of the galaxies, we also derived surface brightness profiles in the broadband g' and r' filters. All surface brightness profiles are shown in Appendix A. We utilized the ellipse package for that purpose. The H α emission in star-forming galaxies is in general very patchy and irregular making it difficult for ellipse to locate the galaxy center and fit ellipses to the flux distribution. To overcome this problem we fit ellipses in the much smoother r' -band images first, defining the geometric parameters of all ellipses in these frames and subsequently applying the same ellipses to the aligned g' -band and H α +NII frames. This way we were able to measure the azimuthally averaged surface brightness level

in all three frames at the exact same position of each galaxy, allowing us to directly compare the surface brightness profiles for both the stellar and the ionized gaseous component of the galaxy disks and reveal any systematic differences in the corresponding light distributions. To quantify these differences we define a light concentration parameter based on the $\mu_{r'} = 24$ mag arcsec $^{-2}$ isophote, hereafter r_{24} , similar to Koopmann, Kenney, & Young (2001):

$$C_{30} = \frac{F_{r'}(0.3r_{24})}{F_{r'}(r_{24})}, \quad (13)$$

where $F_{r'}(r_{24})$ is the total r' band flux within the r_{24} isophote and $F_{r'}(0.3r_{24})$ the r' band flux within the $0.3r_{24}$ isophote. In order to compare the optical concentration with the H α emission, we define the H α light concentration parameter analogous:

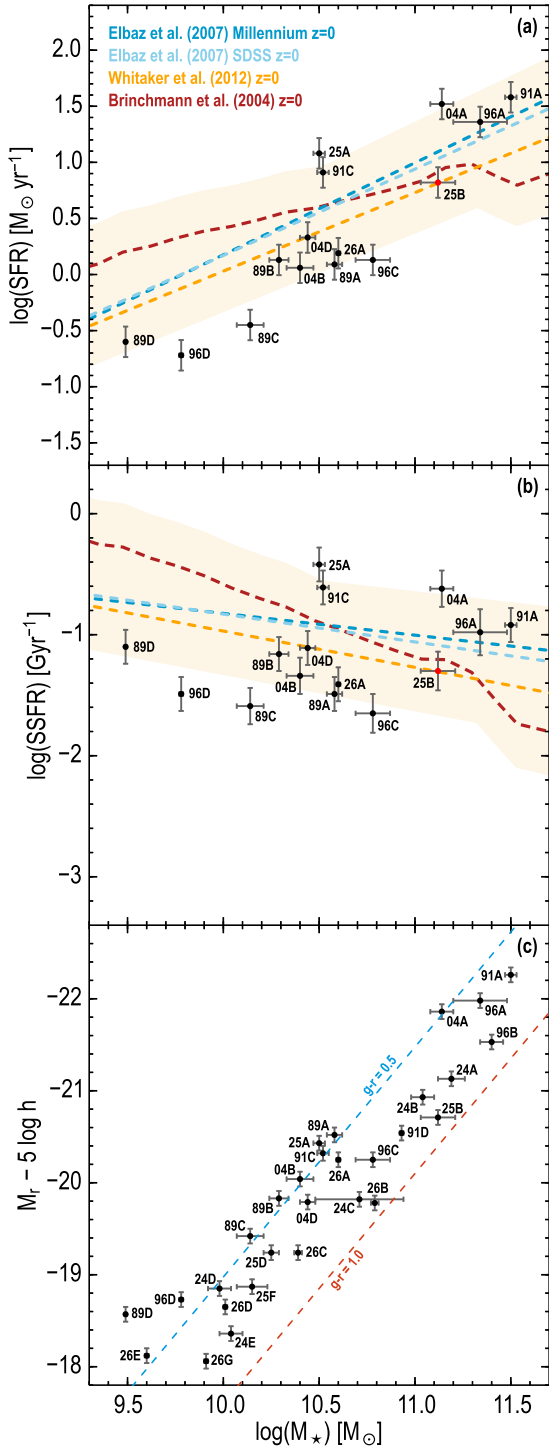


Figure 7. *a*): $\log \text{SFR} - \log M_\star$ plane for all observed HCG member galaxies on the NUV- r' blue sequence. The dashed lines indicate the main sequence of star-forming galaxies as shown in Brinchmann et al. (2004), Elbaz et al. (2007), and Whitaker et al. (2012). The shaded area gives the 1σ scatter of these relations. *b*): Same as panel a), but for the specific star formation rate SSFR. *c*): Absolute magnitude with respect to stellar mass. The dashed lines show the relations for galaxies with $g' - r' = 0.5$ and $g' - r' = 1.0$ based on equation 11.

$$C_{\text{H}\alpha} = \frac{F_{\text{H}\alpha}(0.3r_{24})}{F_{\text{H}\alpha}(r_{24})} \quad (14)$$

where $F_{\text{H}\alpha}(r_{24})$ is the total $\text{H}\alpha$ flux within the r_{24} isophote and $F_{\text{H}\alpha}(0.3r_{24})$ the flux within the $0.3r_{24}$ isophote. Hence, $C_{\text{H}\alpha} = 1$ implies that all $\text{H}\alpha$ emission within r_{24} is located within $0.3r_{24}$ while $C_{\text{H}\alpha} = 0$ indicates that all the $\text{H}\alpha$ emission is located outside of $0.3r_{24}$. Normalizing $C_{\text{H}\alpha}$ by C_{30} then allows for a direct comparison between the light concentration in the stellar and ionized gaseous components. For galaxies with $C_{\text{H}\alpha}/C_{30} > 1$ the $\text{H}\alpha$ emission is more concentrated than the r' band flux while galaxies showing values of $C_{\text{H}\alpha}/C_{30} < 1$ are more concentrated in the r' band with respect to $\text{H}\alpha$. Table 6 lists $C_{\text{H}\alpha}$ and $C_{\text{H}\alpha}/C_{30}$ for all star-forming galaxies in the NUV- r' blue sequence. For those galaxies hosting an AGN, we exclude the central ≤ 0.8 arcsec emission in the $\text{H}\alpha$ frames (cf. section 3.2.1) when computing the $\text{H}\alpha$ light concentration parameter. We compare our measurements with the sample of Koopmann & Kenney (2004) who analyzed $\text{H}\alpha$ profiles of 52 Virgo Cluster spirals.

Figure 9a shows our derived $\text{H}\alpha$ light concentrations with respect to normalized star-formation rate (NMSFR), i.e. the ratio of $\text{H}\alpha$ to r' band flux. Galaxies HCG04A, HCG25A, HCG91C fall in the region of enhanced star-formation in the Koopmann & Kenney (2004) diagram, which is expected since these galaxies are also located in the uppermost envelope of the main sequence of star-forming galaxies as shown in Fig. 7. The HCG galaxies cover a broad range in $C_{\text{H}\alpha}$ from 0.18 to 0.83, with galaxies HCG04A, HCG04D, HCG91A, HCG96C exhibiting values of $C_{\text{H}\alpha} > 0.5$. Figures A1–A5 show surface brightness profiles in g' , r' , and $2.5 \log(\text{H}\alpha + [\text{NII}])$ for all galaxies in Table 6. Vertical dashed lines indicate radii of $0.3 r_{24}$ and r_{24} . We note that for galaxies HCG04A, HCG91A, and HCG96A the steep very central increase of $\text{H}\alpha + [\text{NII}]$ surface brightness is due to the presence of an AGN (unresolved, hence ≤ 0.8 arcsec) which we exclude for the computation of $C_{\text{H}\alpha}$ in these galaxies. Koopmann & Kenney (2004) consider galaxies to be truncated in $\text{H}\alpha$ if the NMSFR drops significantly by a factor of at least 10, i.e. 1.0 dex in the galaxy outskirts ($0.7r_{24} - 1.0r_{24}$). Figure 10 shows radial profiles of the NMSFR for all galaxies in Table 6. Horizontal dashed lines show the mean NMSFR estimated from the integrated $F_{\text{H}\alpha}$ and $F_{r'}$ fluxes within the r_{24} isophote as shown in Fig. 9. Vertical dashed lines show radii at $0.3r_{24}$, $0.7r_{24}$, and $1.0r_{24}$. We see that HCG04B shows a steep cutoff in the NMSFR by 0.76 dex outside r_{24} which could be caused by the interaction with the nearby companion HCG04D. In fact, when looking at the $\text{H}\alpha$ map in Fig. A1, one can see that in the southern part of the galaxy, closer to the companion HCG04D, there are hardly any bright HII regions with respect to the rest of the galaxy. We also note a steep decline in NMSFR for HCG96A in the $0.7r_{24} - 1.0r_{24}$ bin by 0.89 dex. The only other galaxies that show a strong negative gradient in NMSFR are HCG89A and HCG91A. However, in these galaxies the NMSFR rises again towards the outskirts. Based on these measurements and the fact that Koopmann & Kenney (2004) consider a galaxy to be truncated when the NMSFR decreases by a factor of at least 1.0 dex within ($0.7r_{24} - 1.0r_{24}$), technically speaking none of our galaxies shows truncation, although some show significant drops in NMSFR in the galaxy outskirts.

Hence, the high ($C_{\text{H}\alpha} > 0.5$) values derived for some galaxies in our sample can be rather explained by above average central star-formation or a central starburst inducing an overall steep, homogeneous decline of the $\text{H}\alpha$ flux from the center towards the outskirts rather than a sharp cutoff in the outermost parts. Again, HCG96C is

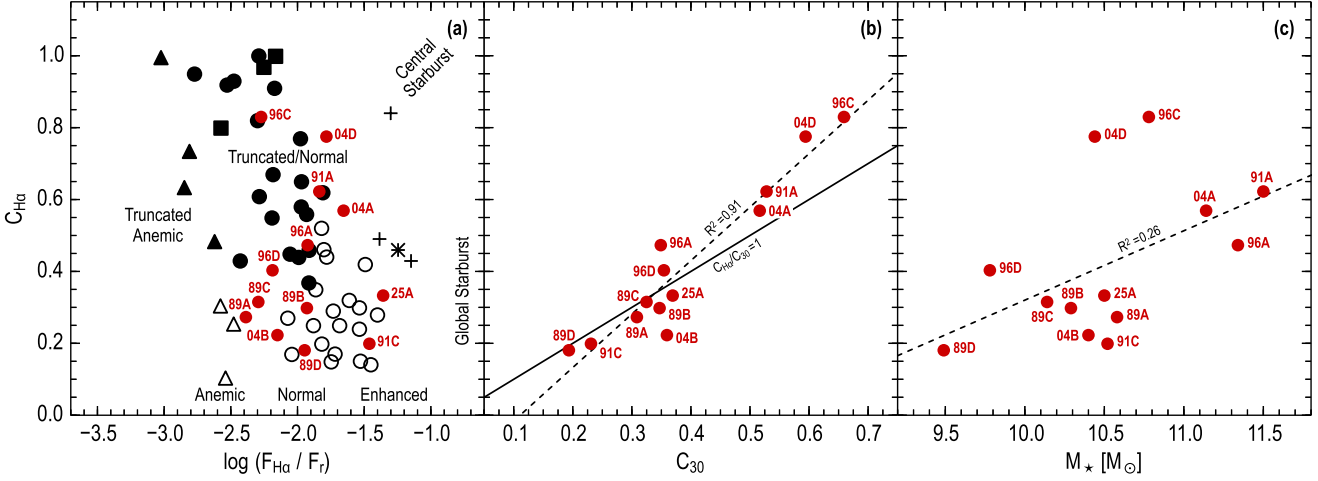


Figure 9. $H\alpha$ light concentration with respect to **a)** the NMSFR (i.e. $\log f_{H\alpha}/f_r$), **b)** the light concentration in the r' band, **c)** stellar mass. Black symbols in panel **a)** show the 52 Virgo Cluster spiral galaxies from the study of Koopmann & Kenney (2004). Full black symbols present galaxies with truncated $H\alpha$ disks while open ones show normal galaxies. The authors also differentiate between anemic (triangles), normal (circles), and enhanced (crosses) star-formation (cf. Fig. 1 Koopmann & Kenney 2004). Red circles show the star-forming galaxies from the present sample. Panel **b)** shows that galaxies that are compact in the r' band, are even more concentrated in $H\alpha$, i.e. $C_{H\alpha}/C_{30} > 1$. The dashed line is a linear least squares fit to the data. The solid line indicates values of $C_{H\alpha}/C_{30} = 1$. Panel **c)** shows that more massive galaxies are more concentrated in $H\alpha$ than less massive ones. The dashed line shows a linear least squares fit to the data.

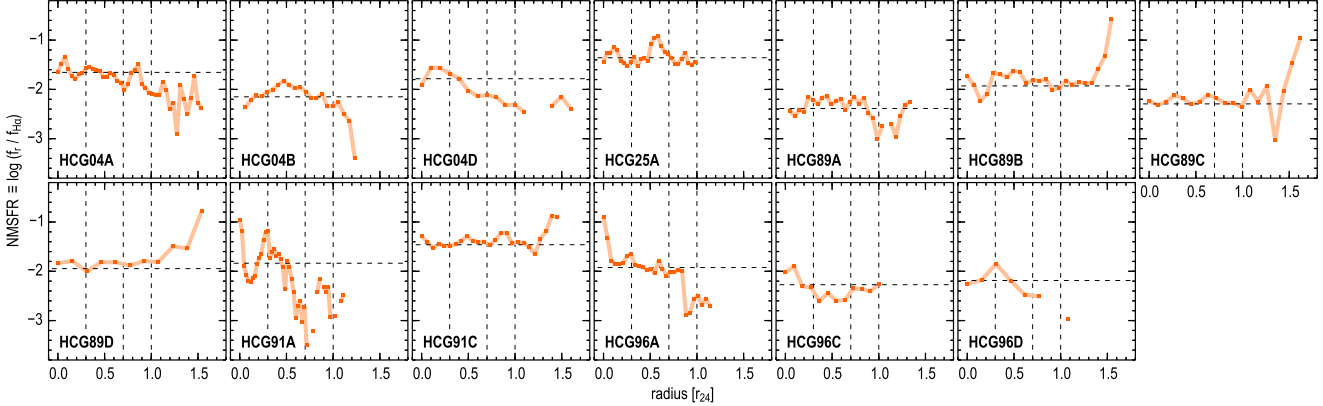


Figure 10. Radial profiles of normalized star-formation rate $NMSFR \equiv \log(f_{H\alpha}/f_r)$ for all galaxies in Table 6. Radii are given in units of r_{24} . Horizontal dashed lines show the mean NMSFR estimated from the integrated $F_{H\alpha}$ and $F_{r'}$ fluxes within the r_{24} isophote. Vertical dashed lines show radii at $0.3r_{24}$, $0.7r_{24}$, and $1.0r_{24}$.

the only galaxy in our sample that seems to be special with respect to the other galaxies we observed, exhibiting a comparatively normal star-formation rate with respect to the Virgo spirals but showing the highest $H\alpha$ concentration from our sample. It is interesting to compare our $H\alpha$ surface brightness profiles with the HI deficiencies of the groups as a whole. Verdes-Montenegro et al. (2001) proposed a scenario where least evolved groups with a low level of interaction have a lower HI deficiency compared to more evolved groups where multiple tidal tails form and gas has been removed from the galaxies. Once the gas has been expelled it can be heated or destroyed more easily, resulting in HI deficient groups. Verdes-Montenegro et al. (2001) found a mean HI deficiency of 0.40 ± 0.07 in HCGs. Table 6 lists the HI deficiencies from Verdes-Montenegro et al. (2001) for our sample revealing that all groups show comparatively low HI deficiencies. This is in agreement with our findings

that we don't see any truncation in the $H\alpha$ disks, suggesting that the groups are in a relatively early stage of their evolution. However, we see clear signs of interaction in HCG91 and HCG96, exhibiting prominent tidal tails. These tails are likely the result of a first encounter in these groups, otherwise we would expect a higher HI gas deficiency in these systems.

Figure 9b shows that there is a clear trend between the r' band light concentration C_{30} and $C_{H\alpha}$ revealing that more compact galaxies in the r' band are systematically more concentrated in $H\alpha$, i.e. $C_{H\alpha}/C_{30} > 1$. The difference in the r' band light concentration parameters C_{30} for different galaxies can be explained by multiple effects. First, the difference in the steepness and overall shape of the surface brightness profiles in the r' band for individual galaxies (e.g. purely exponential disks or multi-component profiles) can obviously change the C_{30} parameter in the sense that galaxy profiles

Table 6. Light concentration parameters and HI deficiencies.

group	galaxy	$C_{H\alpha}$	$C_{H\alpha}/C_{30}^a$	Def _{HI}
HCG04	A ^b ...	0.57	1.10	0.03
	B....	0.22	0.62	
	D....	0.78	1.30	
HCG25	A....	0.33	0.90	0.26
HCG89	A....	0.27	0.88	0.04
	B....	0.30	0.86	
	C....	0.32	0.97	
	D....	0.18	0.93	
HCG91	A ^b ...	0.62	1.18	0.24
	C....	0.20	0.86	
HCG96	A ^b ..	0.47	1.36	<0.17
	C....	0.83	1.26	
	D....	0.40	1.14	

Notes: ^a $C_{H\alpha}/C_{30} > 1$: $H\alpha$ emission is more concentrated than the corresponding r' band flux. ^b Corrected for central AGN.

with a higher Sérsic index will exhibit a higher light concentration parameter. Second, C_{30} also depends on the bulge-to-disk ratio B/T of the individual galaxies, i.e. early-type spirals showing a comparatively high B/T with respect to late-type spirals, will also show a higher C_{30} light concentration parameter. Indeed, from the visual inspection of the r' band frames of galaxies with $C_{30} > 0.5$, we clearly see that all these galaxies host prominent central bulges compared to galaxies with $C_{30} < 0.5$. Thus, the observed trend between C_{30} and $C_{H\alpha}$ could be explained by the fact that galaxies with more massive bulges are able to more effectively attract the gas towards the galaxy center, systematically enhancing star-formation in the center of the galaxies, hence generating larger $C_{H\alpha}/C_{30}$ values. It is also very interesting to compare galaxies in Fig. 9b with Fig. 10. A purely flat profile in NMSFR will put a galaxy on the $C_{H\alpha}/C_{30} = 1$ line in Fig. 9b. Galaxies with $C_{H\alpha}/C_{30} > 1$ on the other hand show an overall declining trend of NMSFR with radius, i.e. there is systematically more $H\alpha$ flux than r' band flux in the galaxy center than in the galaxy outskirts, producing the comparatively high $C_{H\alpha}/C_{30}$ ratios. Finally, Fig. 9c shows a slight trend between stellar mass and $C_{H\alpha}$, more massive galaxies exhibiting a higher $H\alpha$ light concentration. However, there are two galaxies, HCG04D and HCG96C, clearly falling off this sequence, showing a much higher $H\alpha$ light concentration for a given stellar mass. When looking at the corresponding $H\alpha$ maps in Appendix A one can immediately see that the $H\alpha$ flux is indeed very concentrated in these galaxies showing hardly any diffuse distribution of HII regions, but one concentrated source.

To further investigate the morphology of the stellar component we also derived $g'-r'$ color maps, clearly highlighting the distribution of old and young stellar populations within the HCG member galaxies. The color maps were created by considering only sources above 1σ sky noise in each filter. This way we avoid unreliable results caused by low S/N in any of the two passbands. Figures A1–A5 show $H\alpha+[NII]$ maps, $g'-r'$ color maps, and the derived surface brightness profiles for all HCG member galaxies located in the NUV– r' blue sequence.

3.6 Star-forming regions associated with tidal tails

As noted earlier, HCGs provide the ideal environment for the birth of star-forming star clusters and TDGs. Given the continuous interactions present in these groups, gas can be removed efficiently from member galaxies during group evolution. Once expelled, the

gas can cool, self-gravitate and form new stars. Examining the generated $H\alpha+[NII]$ maps from our sample, we see that some groups indeed show $H\alpha$ knots associated with the tidal tails seen in these systems. To identify any star-forming regions we ran SEXTRACTOR from Bertin & Arnouts (1996) on our $H\alpha+[NII]$ maps and considered all objects above 2σ sky noise and a minimum extent of 5 pixels as $H\alpha+[NII]$ sources. Table 7 lists coordinates and $H\alpha+[NII]$ fluxes while Figures 3 and 4 show the corresponding locations of all detected star-forming regions associated with prominent tidal tails in our sample.

In a previous work, Hunsberger et al. (1996) reported the detection of TDG candidates in the tidal tails of HCG26 and HCG96 based on deep R band imaging. However, no $H\alpha$ observations have been carried out for these TDG candidates up to now. The authors mention three TDG candidates in the prominent tidal tail of HCG26 extending towards the northwest. We unambiguously identify the three TDG candidates in our deep r' band images but only see one counterpart, HCG26a, in the corresponding $H\alpha+[NII]$ map above the detection threshold. Hence, the other two TDG candidates detected by Hunsberger et al. (1996) either do not show any significant ongoing star-formation, which would be expected if they formed recently due to the interactions of the host galaxies, or the galaxies are not group members but rather background galaxies in chance projection. This is plausible since Hunsberger et al. (1996) did not confirm the group membership of these TDG candidates spectroscopically. Although HCG26a shows some emission in $H\alpha+[NII]$, its morphological appearance suggests that this galaxy is likely a background galaxy as well, a spiral with a prominent bulge seen edge on. Hence the detected emission in $H\alpha+[NII]$ might be just an artefact due to image processing. The generated $g'-r'$ color maps support the idea that the 3 galaxies are merely background galaxies in chance projection since they are very red compared to the tidal tail they are embedded in (see Fig.B1). We measure $g'-r'$ colors of 1.07 for HCG26a and 0.85 for HCG26b. HCG26c was too faint and diffuse to estimate a reliable colour. Redder colors are expected for these objects if they are located at much higher redshift. Eventually, the true nature of these objects can only be revealed via follow-up spectroscopy.

In HCG96, Hunsberger et al. (1996) claim to detect three TDG candidates as well, one in the eastern, two in the northwestern tidal tail of HCG96A. We only detect two subclumps in our $H\alpha+[NII]$ map of HCG96, one in the eastern and one in the northwestern tail. Unfortunately Hunsberger et al. (1996) don't give RA and DEC coordinates of their detections so it is tedious to match with the detected sources from our work.

HCG91A hosts the most prominent and extended tidal tail in our sample and we detect 10 star-forming regions in $H\alpha+[NII]$ associated with the diffuse light of the tail as seen in the optical. One object is of special interest, HCG91i, located at the very tip of the tail. HCG91i does not show the highest $H\alpha$ luminosity of the detected star-forming regions in HCG91 but it is the most prominent source associated with the tidal tail in the r' band image given its extent, the round, compact morphology, and its location. We measure magnitudes of $r' = 20.14$ and $g' = 21.92$ resulting in a $g'-r'$ color of 1.78. This is comparatively red and suggests that HCG91i hosts an old stellar population (see Fig.B1). However, considering the emission in $H\alpha$, the galaxy also seems to form stars at the present epoch. Given its red colour, we estimate a comparatively high stellar mass of $\log M_{\star} \sim 9.5$ for HCG91i using the equations of Bell et al. (2003).

To estimate the ionized hydrogen mass of all detected star-

forming regions we first computed the $H\alpha$ luminosity of these sources, applying all the corrections highlighted in Sect. 3.2. Then, we derived the corresponding ionizing photon luminosity $Q(H^0)$ considering the relation

$$Q(H^0)[\text{photons s}^{-1}] = 7.31 \times 10^{11} L_{H\alpha}[\text{erg s}^{-1}] \quad (15)$$

from Osterbrock & Ferland (2006). The ionized hydrogen mass can then be computed via

$$M_{\text{HII}}[M_{\odot}] = Q_0 m_p n_e^{-1} \alpha_B^{-1} \quad (16)$$

where m_p is the proton mass, n_e the electron density, and α_B the recombination coefficient (Osterbrock & Ferland 2006). We assumed an electron density of $n_e = 400 \text{ cm}^{-3}$ and $\alpha_B = 2.59 \times 10^{-13} \text{ cm}^3 \text{ s}^{-1}$. Table 7 lists $H\alpha$ luminosities and the derived ionized hydrogen mass of all detected star-forming regions.

4 DESCRIPTION OF INDIVIDUAL GROUPS

HCG04 — Hickson (1982) listed 5 bright galaxies in this group as members. However, HCG04C and HCG04E exhibit discordant redshifts indicating that these galaxies are background galaxies. Also the group membership of the Sb spiral HCG04B is doubtful, since it shows a relative radial velocity of 1074 km s^{-1} with respect to the brightest group member. Peculiar velocities of this magnitude are rather expected in galaxy clusters than groups. The group is dominated by a face-on Sc spiral galaxy (HCG04A) showing two well-defined spiral arms with attached tails exhibiting several knots in $H\alpha$. The spiral arms themselves show multiple star-forming regions arranged like beads on a string à la Barnes & Hernquist (1992). All spectroscopically confirmed member galaxies fall on the NUV- r' blue sequence and are located on the main sequence of star-forming galaxies, also HCG04D, classified as elliptical by Mendes de Oliveira & Hickson (1994). We observed $H\alpha$ emission in every single substructure found in Hunsberger et al. (1998). For HCG04A detailed kinematic data is necessary to determine which HII bright knots belong to the spiral structure and which are tidally formed objects. We find 2 objects in the r' band which are clearly offset from the spiral pattern but don't detect any $H\alpha$ or UV emission for these objects, indicating that these are likely background galaxies. The perturbed spiral arms in HCG04A are signs of a previous galaxy interaction process. In case the interaction partner was another group member of HCG04, the perturbation was either created by a high-speed encounter of HCG04B, or by a slower and more continuous interaction with HCG04D. Martínez et al. (2010) measured emission line ratios in the group member galaxies and classified HCG04D as star-forming, while HCG04A and HCG04B were classified as transition objects between star-forming galaxies and AGNs. Detailed kinematic data of HCG04A together with galaxy interaction simulation with the known properties of HCG04A, B, and D will reveal which galaxy interaction can reproduce the observed perturbation features. Another option could be that a former interaction partner was fully disrupted and has already merged with HCG04A, leaving behind the observed tidal tails.

HCG24 — Hickson et al. (1992) lists 5 bright galaxies in this system. A tidal tail extending from HCG24B towards the east indicates recent interaction. Group members show early-type morphologies, mainly S0 galaxies, all located on the NUV- r' red sequence. We couldn't measure any FUV emission within the group

above the detection limit and any detection in $H\alpha$ is negligible ($s\text{SFR} < -2 \text{ Gyr}^{-1}$).

HCG25 — Originally, Hickson (1982) listed 7 galaxies in this group, however after measuring radial velocities Hickson et al. (1992) noted that HCG25C, HCG25E, and HCG25G show discordant redshifts, leaving only 4 galaxies as members. Except for the SBc spiral HCG25A, all galaxies in the group fall on the NUV- r' red sequence. The most prominent feature in this system is the ongoing interaction between HCG25B and HCG25F, clearly seen as a bridge of stellar material connecting both galaxies. The bridge is made up of two separate filaments extending from HCG25B and blending together when approaching HCG25F. We measure strong $H\alpha$ fluxes for HCG25A and HCG25B. In fact, HCG25A is located at the uppermost envelope of the main sequence of star-forming galaxies. Interestingly, also HCG25B shows comparatively strong $H\alpha$ emission despite its red NUV- r' color and is located on the main sequence of star-forming galaxies. Cluver et al. (2013) detect warm molecular hydrogen in this galaxy and classify it as MOHEG (MOlecular Hydrogen Emission-line Galaxy). HCG25B has also been observed spectroscopically with SDSS and given its $[\text{NII}]/H\alpha$ emission line ratio it can be considered as AGN. However, Cluver et al. (2013) state that AGN activity is unlikely to be responsible for the observed H_2 enhancement and that shock excitation through interaction with the IGM is a plausible mechanism for producing the observed emission. In the $g'-r'$ color map we see a comparatively red, disklike structure in the center of this galaxy. We don't see any $H\alpha$ emission in the bridge filaments above the detection limit indicating that the bridge doesn't show any SF activity. However, we note that based on the redshift of the system and the narrowband filter transmissivity, the $H\alpha$ detection limit is very low for this system (see Fig. 1). Only spatially resolved spectroscopy will reveal the ionization mechanism present in this galaxy and shed light on the origin of the strong $H\alpha + [\text{NII}]$ flux measured in the present work.

HCG26 — This compact group is dominated by an edge-on Scd spiral galaxy (HCG26A) interacting with an E0 elliptical (HCG26B) and shows a tidal tail extending from the spiral towards the northwest. Hickson et al. (1992) lists a total of 7 spectroscopically confirmed group members. Hunsberger et al. (1996) have studied this group in detail in the R band and claim to detect three tidal dwarf galaxies in the tail. Since we don't see any $H\alpha$ emission within the tail, it could be a stellar stream made up of a purely old stellar population as seen around the MW and M31. Given the compactness of the system, it is unclear to which galaxy the tidal arm belongs. Based on its position and alignment it could have formed from HCG26B, assuming that HCG26B was moving perpendicular with respect to the disk of HCG26A. Kinematic data is needed to verify the origin of the tidal feature.

HCG89 — This group is made up of four late-type spiral galaxies, all located on the NUV- r' blue sequence. The group members do not show strong signs of gravitational interaction. HCG89D is the galaxy with the lowest stellar mass and bluest color in our sample. Coziol et al. (2004) studied the emission-line properties of both HCG89A and HCG89B, classifying both galaxies as star-forming galaxies, showing no AGN activity. From our $H\alpha$ measurements we derive that HCG89B and HCG89D fall on the main sequence of star-forming galaxies while HCG89A and HCG89C both fall below the main sequence.

HCG91 — Hickson et al. (1992) lists 4 group members in this group, of which only three, HCG91A, HCG91C, and HCG91D fall in our FOV. The system is dominated by a SBc face-on spiral galaxy (HCG91A) interacting with a much fainter SB0 companion (HCG91D) and shows a prominent tidal tail extending from

Table 7. TDG candidates.

group	source	α_{2000}	δ_{2000}	$\log F_{\text{H}\alpha+\text{NII}}$ [erg s ⁻¹ cm ⁻²]	$\log L_{\text{H}\alpha}$ [erg s ⁻¹]	$\log \text{SFR}_{\text{H}\alpha}^b$ [M _⊙ year ⁻¹]	$\log M_{\text{HII}}$ [M _⊙]	distance ^a [kpc]
HCG26	a	03 21 54.70	-13 38 34.5	-15.41	38.82	-2.45	3.60	17
	b	03 21 54.58	-13 38 25.3	22
	c	03 21 54.75	-13 38 18.4	26
HCG91	a	22 09 04.13	-27 48 08.7	-15.04	38.95	-2.32	3.72	26
	b	22 09 03.64	-27 48 17.4	-15.45	38.53	-2.74	3.31	27
	c	22 09 09.17	-27 49 13.0	-14.89	39.09	-2.18	3.86	20
	d	22 09 09.60	-27 49 13.0	-14.66	39.33	-1.94	4.10	22
	e	22 09 11.04	-27 49 12.8	-14.86	39.12	-2.15	3.89	28
	f	22 09 13.09	-27 48 01.1	-15.25	38.73	-2.54	3.50	38
	g	22 09 14.02	-27 47 54.1	-15.03	38.95	-2.32	3.72	45
	h	22 09 10.22	-27 47 05.9	-15.41	38.57	-2.70	3.34	46
	i	22 09 06.98	-27 46 42.4	-14.98	39.00	-2.27	3.77	54
	j	22 09 06.30	-27 46 35.5	-14.85	39.13	-2.14	3.90	58
HCG96	a	23 27 56.73	08 47 21.0	-15.66	38.50	-2.77	3.27	22
	b	23 28 01.89	08 46 58.7	-15.92	38.24	-2.93	3.02	46

Notes: ^a Distances measured from the peak of the surface brightness distribution in the brightest group galaxies HCG26A, HCG91A and HCG96A.

HCG91A to the east. HCG91A and HCG91C are both located on the NUV- r' blue sequence and fall on the main sequence of star-forming galaxies, while HCG91D doesn't show any emission in H α or FUV, falling on the NUV- r' red sequence. Although Cluver et al. (2013) detect warm molecular hydrogen in galaxies HCG91A and HCG91C, which, based on their work, can only be explained by shock excitation, these shocks do not seem to suppress star-formation in both galaxies. HCG91A hosts a prominent tidal tail clearly visible in our deep r' band image. The tail splits into two subcomponents pointing northeast. We find several H α knots along the tidal tail indicating active, interaction-induced star-formation. We report a yet unidentified TDG at the tip of the tidal tail in HCG91. Given the low HI deficiency of the system, the tidal tail very likely originates from a first encounter in this group. Indeed, Bitsakis et al. (2014) classify the system as dynamically young.

HCG96 — HCG96 is made up of 4 members, dominated by a Sc galaxy (HCG96A) interacting with an Sa companion (HCG96C) and shows two long, filamentary tidal tails extending from HCG96A to the east and to the northwest. Based on the $g'-r'$ color map for this galaxy, we note that the the northwestern tail exhibits a much bluer color than the eastern one. This is in agreement with the work of Verdes-Montenegro et al. (1997) who have studied the system in detail and showed a similar result. Cluver et al. (2013) have found molecular hydrogen H_2 in galaxies HCG96A and HCG96C. HCG96C is the only galaxy from our sample that is located in the NUV- r' green valley (see Fig. 5) and shows the highest H α concentration within our sample. Torres-Flores et al. (2013) showed that this galaxy also deviates from the baryonic Tully-Fisher relation. Cluver et al. (2013) do not classify HCG96C as a MOHEG, hence shocks do not seem to be the mechanism suppressing star-formation in this galaxy. Given its vicinity to HCG96A, a likely explanation for the suppressed star-formation in this galaxy could be the ongoing interaction with the massive nearby galaxy HCG96A. However, we do not see a sign of gas disk truncation in this object (see Fig. 10). Similar to HCG91, the group shows a comparatively low HI deficiency and the tidal tails likely originate from a first encounter in this group. The system is also classified as dynamically young by Bitsakis et al. (2014).

5 CONCLUSION

We have observed a sample of seven compact groups from the well-known catalog of Hickson (1982) in g' , r' , and a narrow-band filter located at the redshifted H α line to study the star-forming properties of these groups. Given the high-density environment in compact groups and the prevalence of galaxy-galaxy interactions within these aggregates, star-formation of member galaxies is expected to be strongly affected by the group environment. In contrast to the galaxy cluster environment, where the star-forming properties of individual members are mostly affected by the overall cluster potential, star-formation rates of galaxies in compact groups are more prone to ongoing galaxy-galaxy interactions. Hence, a smooth trend of star-forming properties with respect to group mass is not expected, whereas this is observed in galaxy clusters. To test these assumptions, we investigated the star-forming properties of our sample by measuring both integrated star-formation rates of the galaxies as a whole, and in 2-D, by generating H α maps and constructing azimuthally averaged H α surface brightness profiles. Since the gas-disks of star-forming galaxies are easily distorted by ongoing galaxy-galaxy interactions, clear signs of interactions such as truncated H α profiles are then expected to be observed. We sum up our findings as follows:

1. Group member galaxies are found in two pronounced and distinct sequences in the NUV- r' vs. absolute r' band magnitude plane, unambiguously separating blue star-forming galaxies from passively evolving, quiescent red galaxies following the well-defined blue and red sequences for SDSS galaxies in the local universe. From a total of 23 bright HCG member galaxies in our sample (for which we have NUV data), we find 12 galaxies ($\sim 52\%$) located in the NUV- r' blue sequence while we find 10 ($\sim 44\%$) located in the red sequence.

2. We find only one galaxy ($\sim 4\%$), HCG96C, located in the NUV- r' green valley. Given its vicinity to the brightest group galaxy HCG96A, HCG96C is undergoing strong galaxy-galaxy interaction causing star-formation to be quenched and consequently moving the galaxy from the blue star-forming sequence towards the red, passive sequence. Interestingly, this galaxy shows also the highest H α concentration within our sample.

3. Except for 3 galaxies all galaxies are located within the 1 σ confidence intervals of the main sequence of star-forming galaxies

in the local universe. Only HCG89C, HCG96C, and HCG96D fall below the main sequence. We do not see any systematic enhancement of the global star-formation rate in star-forming HCG member galaxies.

4. Despite being located on the NUV- r' red sequence, we measure a comparatively high $H\alpha$ star-formation rate for the elliptical galaxy HCG25B, falling on the main sequence of star-forming galaxies. The $g'-r'$ color map reveals a comparatively red, disk-like structure in the central region of this galaxy.

5. We get a good agreement between $H\alpha$ and FUV star-formation rates for the brightest star-forming galaxies in our sample, while fainter galaxies show higher star-formation rates in FUV compared to $H\alpha$.

6. We find 13 star-forming regions associated with the tidal tails of HCG26, HCG91, and HCG96. While we find only one $H\alpha$ source in the tail of HCG26 and 2 in the tidal tails of HCG96, we detect 10 $H\alpha$ sources along the tidal tails of HCG91. In particular we find a prominent object, HCG91i, in both $H\alpha$ and the broadband r' image at the tip of the extended tidal tail in HCG91.

7. Based on radial profiles of the normalized star-formation rate (NMSFR) and the truncation criterion from Koopmann & Kenney (2004), none of our galaxies show $H\alpha$ disk truncation, although some galaxies (HCG04B, HCG91A, HCG96A) show a significant drop in the NMSFR in the galaxy outskirts. Given our findings and the comparatively low HI deficiencies of the observed groups, we argue that these systems did not experience a lot of galaxy-galaxy interactions so far. Groups that show prominent tidal tails (HCG91A, HCG96A) are likely having their first encounter.

8. We find a clear trend that more massive galaxies show a higher concentration in the azimuthally averaged $H\alpha$ surface brightness profiles and that galaxies showing a high light concentration in the r' band show a systematically higher light concentration in $H\alpha$.

ACKNOWLEDGMENTS

This work is based on observations obtained at the Southern Astrophysical Research (SOAR) telescope, which is a joint project of the Ministério da Ciência, Tecnologia, e Inovação (MCTI) da República Federativa do Brasil, the U.S. National Optical Astronomy Observatory (NOAO), the University of North Carolina at Chapel Hill (UNC), and Michigan State University (MSU). This work has made use of IRAF which is distributed by the National Optical Astronomy Observatories, which are operated by the Association of Universities for Research in Astronomy, Inc., under cooperative agreement with the National Science Foundation. We want to thank the anonymous referee who helped to improve the paper. We also want to thank Sergio Torres-Flores and Claudia Mendes de Oliveira for helpful discussions. PE acknowledges support from FONDECYT through grant 3130485. SP acknowledges support from the European Research Council under the European Union's Seventh Framework Programme (FP7/2007-2013)/ERC Grant agreement 278594 - Gas Around Galaxies.

REFERENCES

Alatalo, K., Appleton, P. N., Lisenfeld, U. et al. 2014, ApJ, 795, 159

- Barnes, J. E., & Hernquist, L. 1992, Nature, 360, 715
 Bell, E. F., McIntosh, D. H., Katz, N. et al. 2003, ApJS, 149, 289
 Bertin, E., & Arnouts, S. 1996, A&AS, 117, 393
 Bitsakis, T., Charmandaris, V., Appleton, P. N. et al. 2014, A&A, 565, 25
 Brinchmann, J. et al. 2004, MNRAS, 351, 1151
 Calzetti, D., Kinney, A. L., & Storchi-Bergmann, T. 1994, ApJ, 429, 582
 Cardelli, J. A., Clayton, G. C., & Mathis, J. S. 1989, ApJ, 345, 245
 Cluver, M. E., Appleton, P. N., Ogle, P. et al. 2013, ApJ, 765, 93
 Coziol, R., Brinks, E., & Bravo-Alfaro, H. 2004, AJ, 128, 68
 Draper, P. W., Berry, D. S., Jenness, T. et al. 2009, ASPC, 411, 575
 Elbaz, D. et al. 2007, A&A, 468, 33
 Hamuy, M., Walker, A. R., Suntzeff, N. B. et al. 1992, PASP, 104, 533
 Hamuy, M., Suntzeff, N. B., Heathcote, S. R. et al. 1994, PASP, 106, 566
 Hickson, P. 1982, ApJ, 255, 382
 Hickson, P., Mendes de Oliveira, C., Huchra, J. P. et al. 1992, ApJ, 399, 353
 Hunsberger, S. D., Charlton, J. C., & Zaritsky, D. 1996, ApJ, 462, 50
 Hunsberger, S. D., Charlton, J. C., & Zaritsky, D. 1998, ApJ, 505, 536
 Ivezić, Ž., Smith, J. A., Miknaitis, G. et al. 2007, AJ, 134, 973
 Kennicutt, R. C. J., Armus, L., Bendo, G. et al. 2003, PASP, 115, 928
 Kennicutt, R. C. J., Hao, C.-N., Calzetti, D. et al. 2009, ApJ, 703, 1672
 Kennicutt, Jr., R. C., Evans, II. N. J. 2012, ARA&A, 50, 531
 Martínez, M. A., Del Olmo, A., Coziol, R. et al. 2010, AJ, 139, 1199
 Mendes de Oliveira, C., & Hickson, P. 1994, ApJ, 427, 684
 Osterbrock, D. E., Ferland, G. J. 2006, *Astrophysics of gaseous nebulae and active galactic nuclei*, 2nd. ed., University Science Books
 Ryder, S. D., Murrowood, C. E., & Stathakis, R. A. 2006, MNRAS, 369, L32
 Salim, S., Rich, R. M., Charlot, S. et al. 2007, ApJS, 173, 267
 Schlafly, E. F., & Finkbeiner, D. P. 2011, ApJ, 737, 103
 Torres-Flores, S., Mendes de Oliveira, C., Plana, H. et al. 2013, MNRAS, 432, 3085
 van Dokkum, P. G. 2001, PASP, 113, 1420
 Verdes-Montenegro, L., Del Olmo, A., Perea, J. et al. 1997, A&A, 321, 409
 Verdes-Montenegro, L., Yun, M. S., Williams, B. A. et al. 2001, A&A, 377, 812
 Whitaker, K. E. et al. 2012, ApJL, 754, L29
 Wright, E. L. 2006, PASP, 118, 1711
 Wyder, T. K., Martin, D. C., Schiminovich, D. et al. 2007, ApJS, 173, 293
 Laher, R. R., Gorjian, V., Rebull, L. M. et al. 2012, PASP, 124, 737
 Oke, J. B., & Gunn, J. E. 1983, ApJ, 266, 713
 Garn, T., & Best, P. N. 2010, MNRAS, 409, 421
 Kashino, D., Silverman, J. D., Rodighiero, G. et al. 2013, ApJL, 777, L8
 Iglesias-Páramo, J., & Vilchez, J. M. 2001, ApJ, 550, 204
 Tully, R. B. 1987, ApJ, 321, 280
 Diaferio, A., Geller, M. J., Ramella, M. 1994, AJ, 107, 868

- Barnes, J. 1985, MNRAS, 215, 517
Bode, P. W., Cohn, H. N., Lugger, P. M. 1993, ApJ, 416, 17
Renaud, F., Boily, C. M., Naab, T., Theis, C. 2009, ApJ, 706, 67
Bitsakis, T., Charmandaris, V., Le Floch, E. et al. 2010, A&A, 517, 75
Desjardins, T. D. et al. 2013, ApJ, 763, 121
Nolthenius, R. 1993, ApJSS, 85, 1
Abell, G. O., Corwin, H. G. J., & Olowin, R. P. 1989, ApJSS, 70, 1
Serra, P., Koribalski, B., Duc, P. A. et al. 2013, MNRAS, 428, 370
Duc, P. A. 2012, *Dwarf Galaxies: Keys to Galaxy Formation and Evolution*, 305
Koopmann, R. A., Kenney, J. D. P., & Young, J. 2001, ApJS, 135, 125
Koopmann, R. A., & Kenney, J. D. P. 2004, ApJ, 613, 866
Véron-Cetty, M. P., & Véron, P. 2010, A&A, 518, 10

APPENDIX A: H α MAPS, COLOR MAPS, AND SURFACE BRIGHTNESS PROFILES OF HCG MEMBER GALAXIES

APPENDIX B: COLOR MAPS FOR THE GROUPS AS A WHOLE

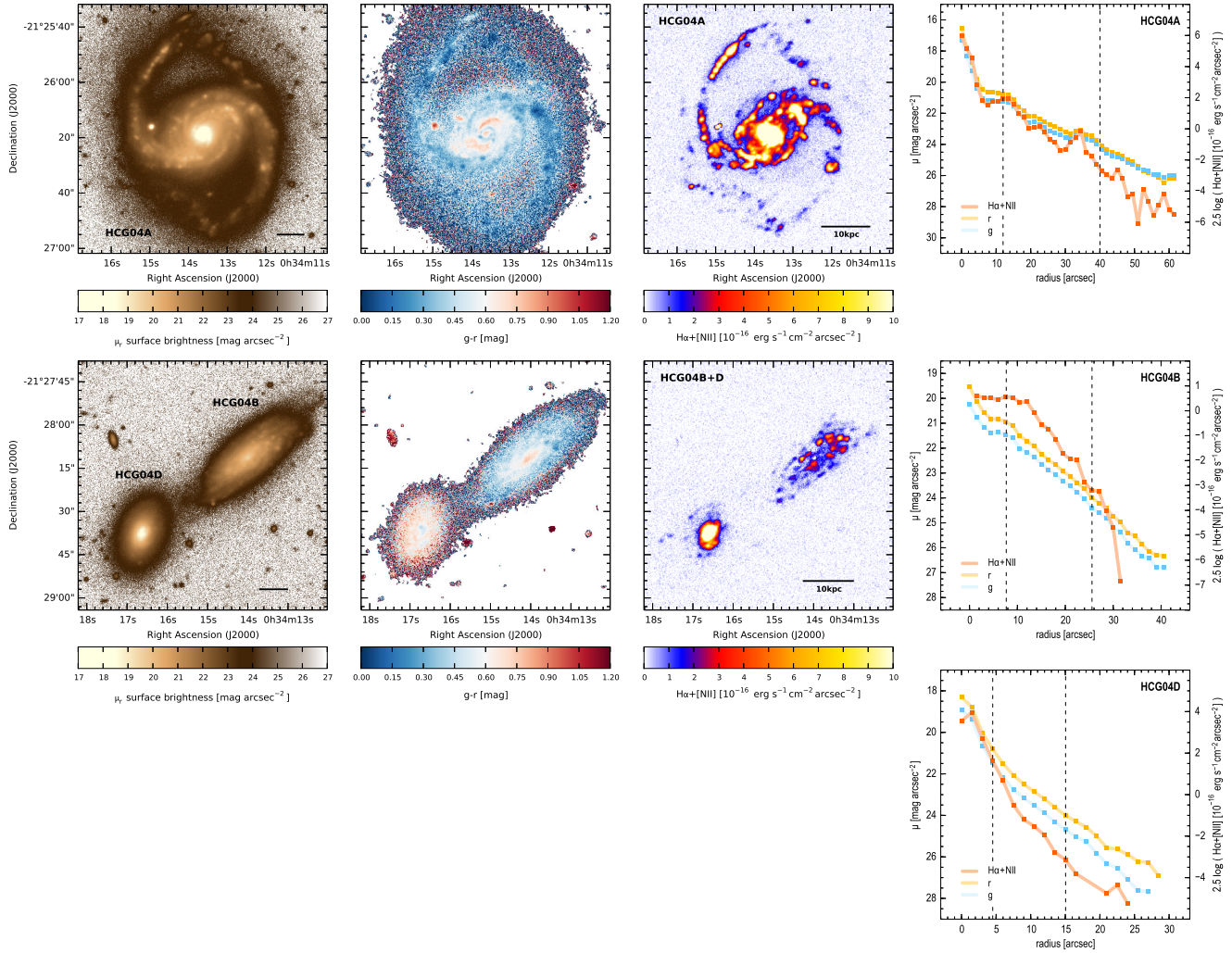


Figure A1. r' band images, $g'-r'$ color maps, $H\alpha+[NII]$ maps and radial profiles for HCG04A and HCG04B+D. Horizontal scales show 10 arcsec in the r' band and 10kpc in the $H\alpha+[NII]$ maps. Applying all corrections and conversion from Sect. 3.2, an $H\alpha+[NII]$ flux of $10^{-16} \text{ erg s}^{-1} \text{ cm}^{-2} \text{ arcsec}^{-2}$ corresponds to a surface star-formation rate of $\Sigma_{\text{SFR}} = 6.34 \cdot 10^{-3} M_{\odot} \text{ yr}^{-1} \text{ kpc}^{-2}$. We note, however, that this conversion is likely to vary within the galaxy. The sky noise (1σ) corresponds to $0.20 \cdot 10^{-16} \text{ erg s}^{-1} \text{ cm}^{-2} \text{ arcsec}^{-2}$. Radial profiles are shown in surface brightness for g' and r' , and $2.5 \log(H\alpha+[NII])$ for $H\alpha$. Vertical dashed lines indicate radii of $0.3 r_{24}$ and r_{24} (see text).

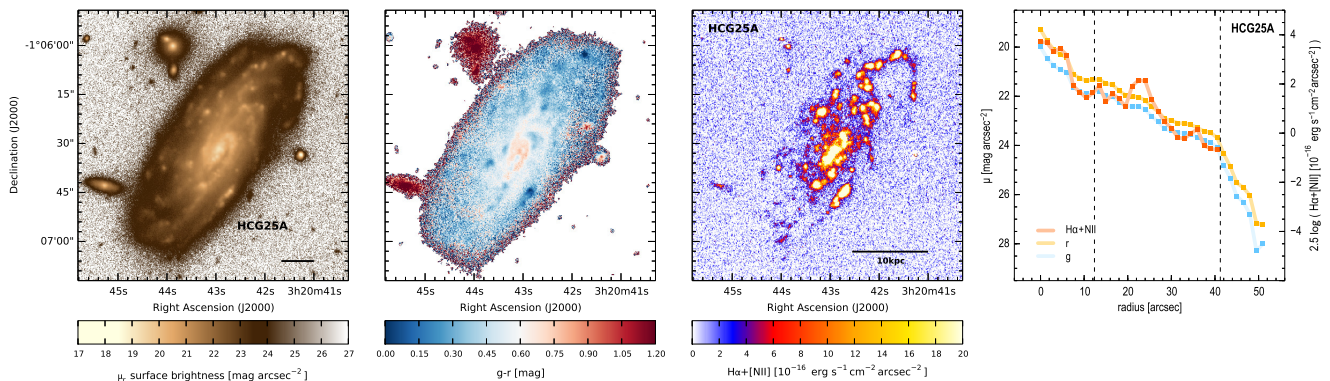


Figure A2. Same as Fig. A1 but for HCG25A. A flux of $10^{-16} \text{ erg s}^{-1} \text{ cm}^{-2} \text{ arcsec}^{-2}$ corresponds to a surface star formation rate of $\Sigma_{\text{SFR}} = 6.76 \cdot 10^{-3} M_{\odot} \text{ yr}^{-1} \text{ kpc}^{-2}$. The sky noise (1σ) corresponds to $1.56 \cdot 10^{-16} \text{ erg s}^{-1} \text{ cm}^{-2} \text{ arcsec}^{-2}$.

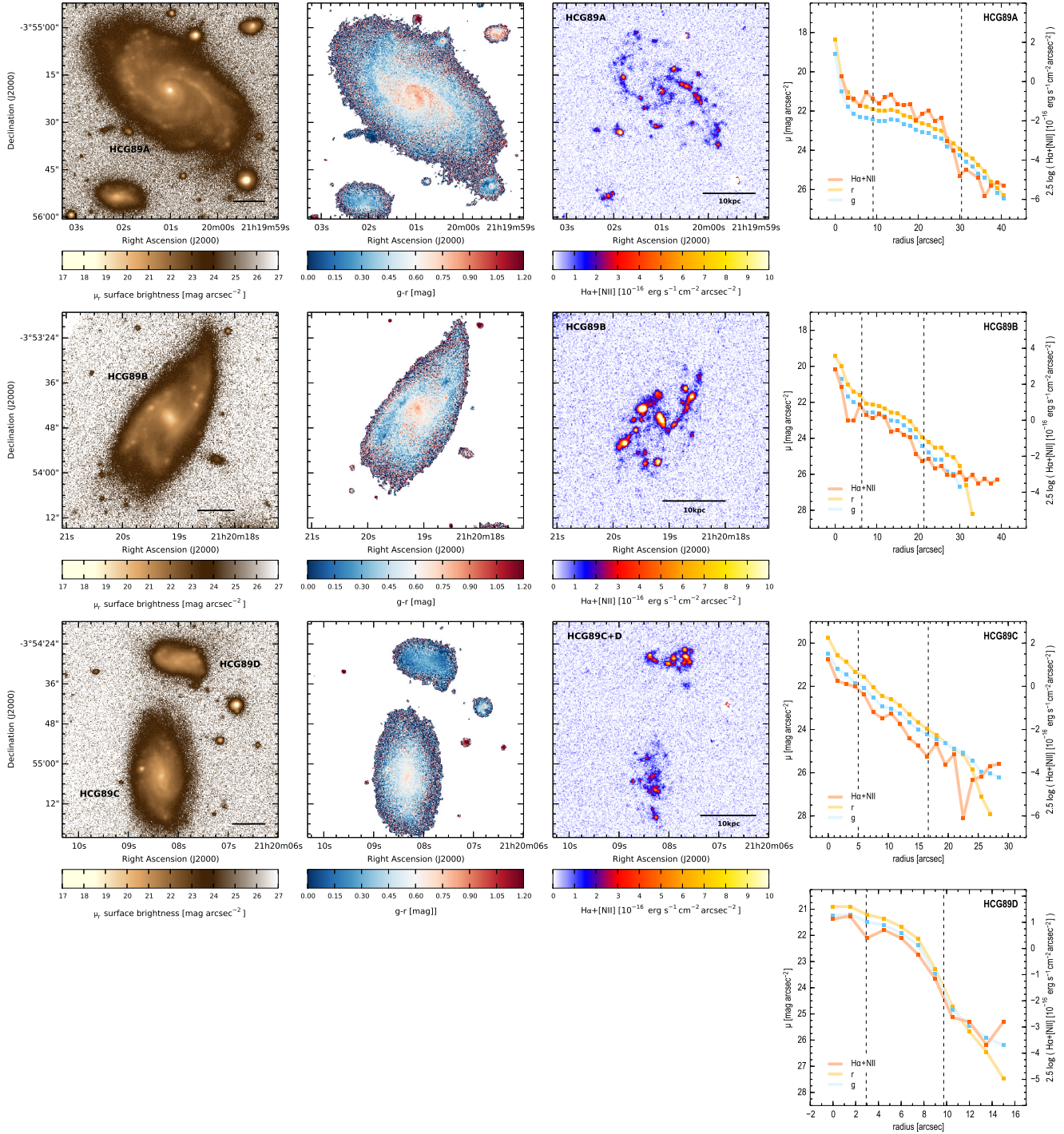


Figure A3. Same as Fig. A1 but for HCG89A, HCG89C+D, and HCG89B. A flux of 10^{-16} erg s⁻¹ cm⁻² arcsec⁻² corresponds to a surface star-formation rate of $\Sigma_{\text{SFR}} = 6.88 \cdot 10^{-3} M_{\odot} \text{ yr}^{-1} \text{ kpc}^{-2}$. The sky noise (1σ) corresponds to $0.37 \cdot 10^{-16}$ erg s⁻¹ cm⁻² arcsec⁻².

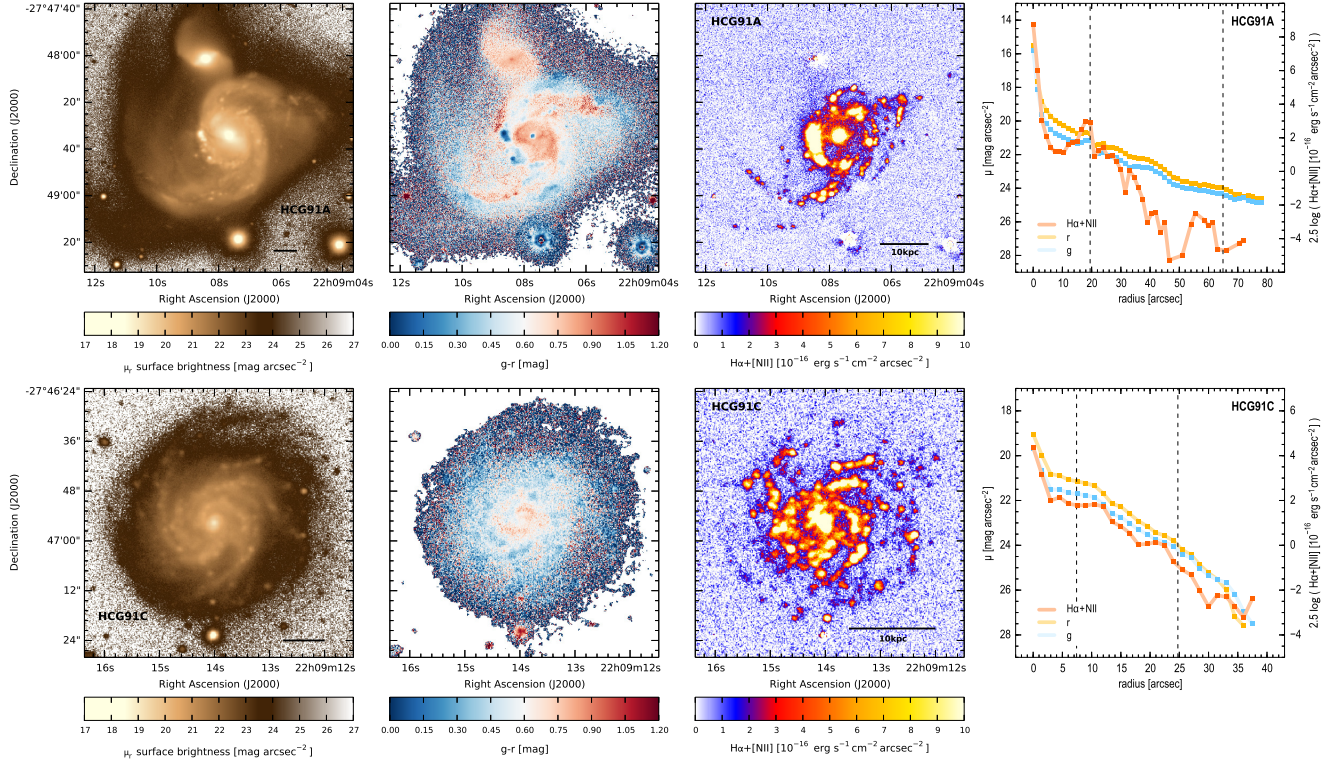


Figure A4. Same as Fig. A1 but for HCG91A and HCG91C. A flux of 10^{-16} erg s $^{-1}$ cm $^{-2}$ arcsec $^{-2}$ corresponds to a surface star-formation rate of $\Sigma_{\text{SFR}} = 6.20 \cdot 10^{-3} M_{\odot} \text{ yr}^{-1} \text{ kpc}^{-2}$. The sky noise (1σ) corresponds to $0.62 \cdot 10^{-16}$ erg s $^{-1}$ cm $^{-2}$ arcsec $^{-2}$.

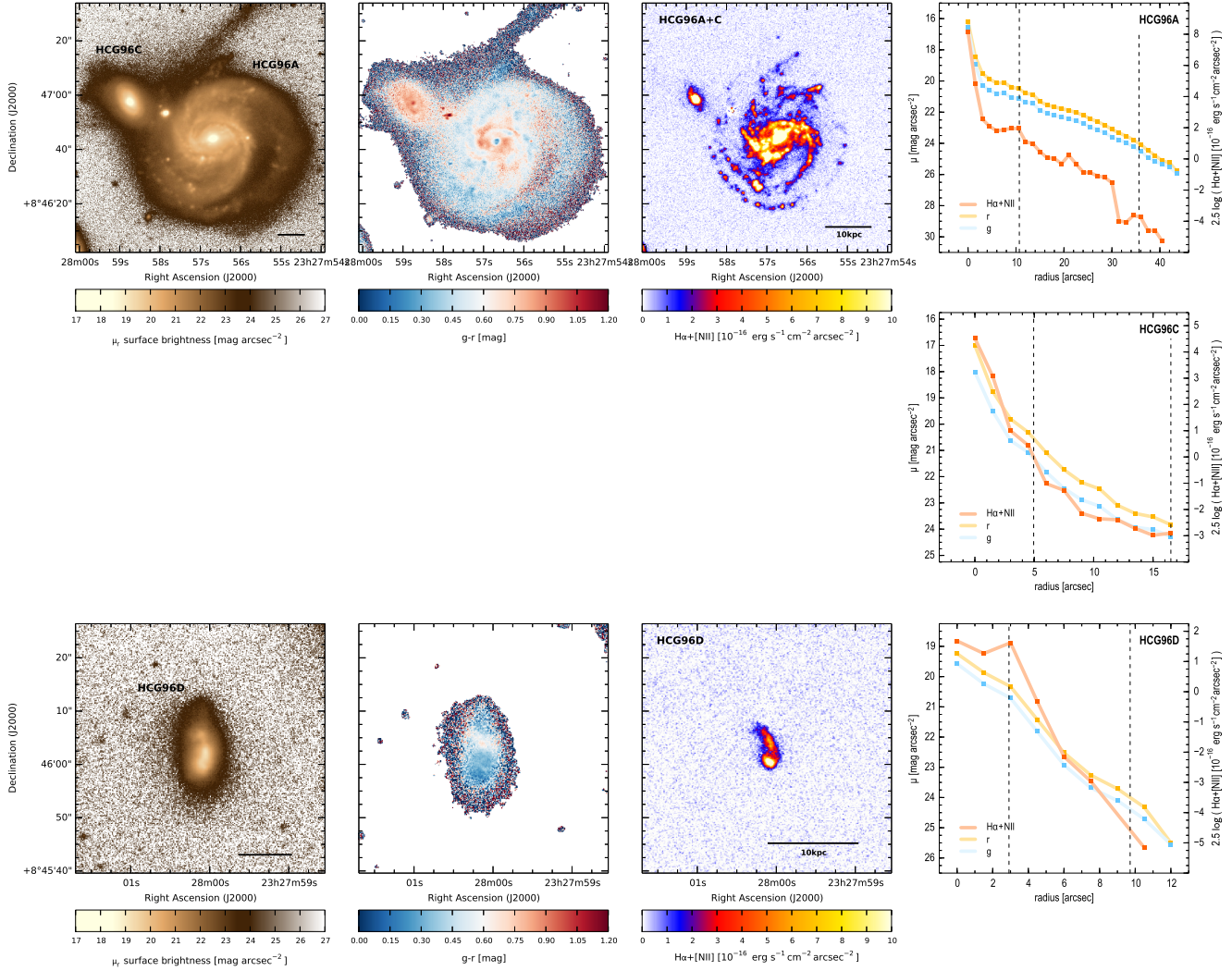


Figure A5. Same as Fig. A1 but for HCG96A+C+D. A flux of $10^{-16} \text{ erg s}^{-1} \text{ cm}^{-2} \text{ arcsec}^{-2}$ corresponds to a surface star-formation rate of $\Sigma_{\text{SFR}} = 6.87 \cdot 10^{-3} M_{\odot} \text{ yr}^{-1} \text{ kpc}^{-2}$. The sky noise (1σ) corresponds to $0.28 \cdot 10^{-16} \text{ erg s}^{-1} \text{ cm}^{-2} \text{ arcsec}^{-2}$.

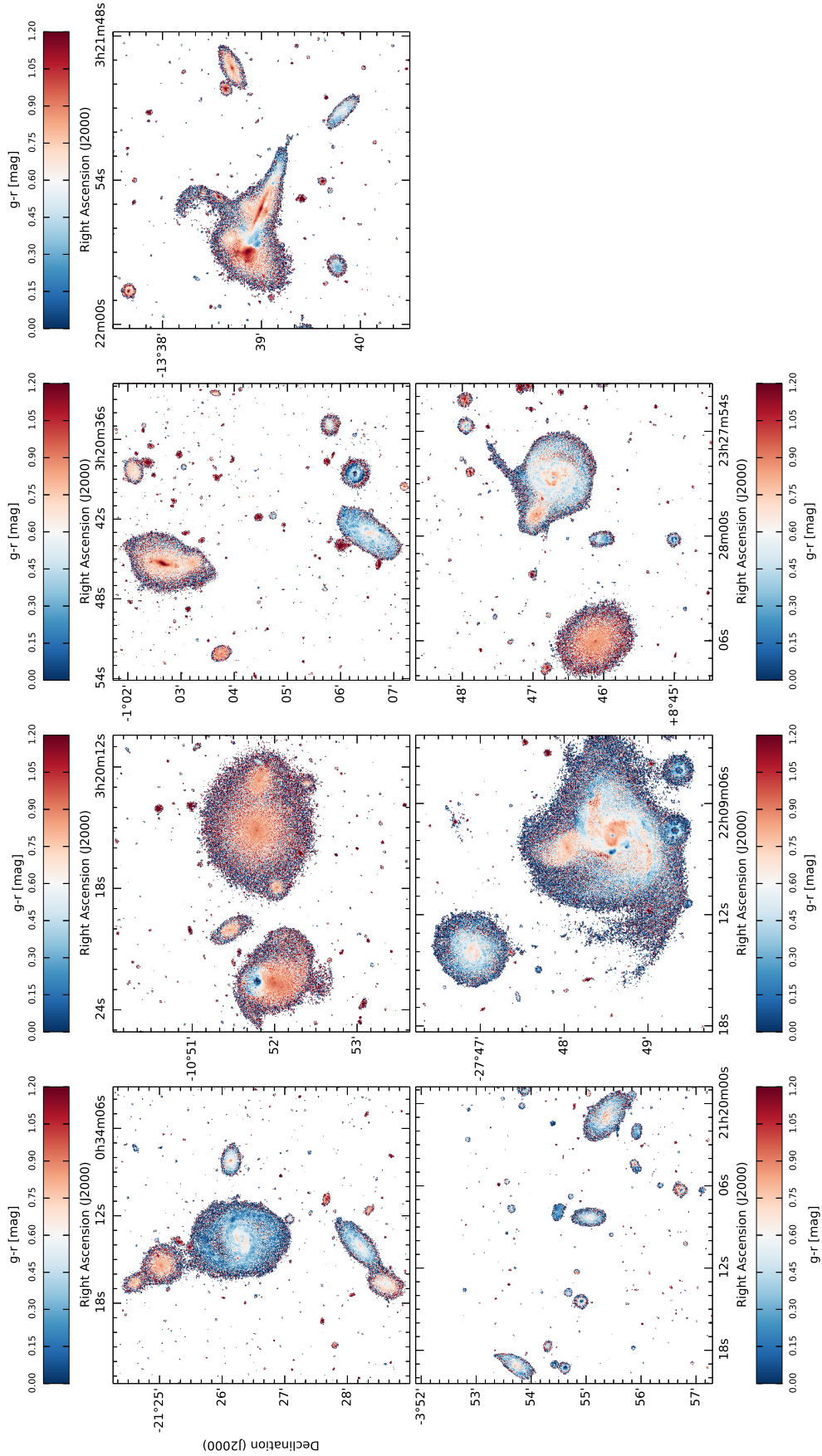


Figure B1. $g'-r'$ color maps for all observed HCGs. Only sources above 1σ sky noise in both filters are shown.